# Strengthening Mechanisms of Semi-Coherent Boundaries between $Al_8Mn_4Y$ and the Mg Matrix in Magnesium Alloys

Yanfei Chen[a], Zhengqiang Zhu[a,*], M. Amir Siddiq[b], Ke Li[a], Jixue Zhou[c]
a. School of Advanced Manufacturing, Nanchang University, Nanchang 330031, PR China.
b. School of Engineering, University of Aberdeen, Aberdeen, AB24 3UE, UK.
c. Advanced Materials Institute, Shandong Academy of Sciences, Ji'nan 250014, PR China.

## Abstract

The dominant failure mode in Mg alloys has been reported to be cracking at phase or grain boundaries in the past. This shows the importance of enhancing these boundaries to improve the strength and ductility of Mg alloy. However, producing strongly bonded twin boundaries in Mg alloys is challenging. This work addresses this challenge and presents a novel method to enhance the bonding between intermetallics and the matrix by forming semi-coherent boundaries. By employing transmission electron microscopy (TEM), a previously unexplored intermetallic compound (IMC), $Al_8Mn_4Y$, has been identified and systematically investigated. The orientation relationship between lattices of Al8Mn4Y and Mg matrix reveals that the angle between $\{0\bar{1}0\}$Al8Mn4Y and $\{000\bar{1}\}$α-Mg planes is approximately 3.9°. Furthermore, typical lattice mismatches are observed after every four $Al_8Mn_4Y$ lattices along the $<010>_{Al8Mn4Y}$ direction at the bonding interface, demonstrating their semi-coherent relationship. Subsequently, the mechanical properties of $Al_8Mn_4Y$ are measured using nanoindentation. While the corresponding impact of Y-containing intermetallics on the mechanical properties of the alloy is also evaluated through tensile tests and fracture analyses. The results reveal that the refinement of conventional intermetallics originally present in the alloy along with the newly generated Y-containing particles and the corresponding semi-coherent boundaries, effectively reduces the stress concentration and mitigates cracking at phase and grain boundaries. This reduction in stress concentration and crack mitigating effect has been found to contribute to the simultaneous enhancement of strength and ductility in Mg alloys. The effects of Y on the elastic and plastic deformation of Mg alloys are also quantified using four individual contributions, while the underlying mechanisms causing simultaneous enhancement of strength and ductility are elucidated. These new insights offer great opportunities to design strategies for future Mg alloys.

**Keywords:** Rare-earth; Magnesium alloy; Yttrium (Y); Semi-coherent boundaries; Strengthening mechanisms

## 1. Introduction

The demand to reduce the weight of components, particularly in automotive, aviation/aerospace, and military applications, has sparked interest in the use of Mg alloys as lightweight material [1]. However, Mg is a soft material with low strength. Moreover, the hexagonal close-packed (HCP) structure of Mg makes the activation of non-basal slip and twinning challenging, resulting in poor ductility of Mg alloys [2]. These limitations make conventional Mg alloys fail to meet the requirements of practical applications in terms of strength, ductility, and heat resistance [3].

To improve the strength and ductility of Mg alloys, alloying elements are added. As a result, well-designed and finely distributed intermetallic compounds (IMCs) are formed within the alloy, which refine the grains, increase dislocation density, and impede dislocation motion [4]. However, most intermetallic compounds in Mg alloys are

* Corresponding author at: School of Advanced Manufacturing, Nanchang University, Nanchang 330031, PR China;
E-mail: 350906320003@email.ncu.edu.cn (Zhengqiang Zhu); Tel: +086-18396868965.

thermally unstable, and their interfacial relationships with the Mg matrix are incoherent [5]. The corresponding phase boundaries (i.e., boundaries between IMCs and the Mg matrix) are weakly bonded. During the deformation, stress concentrations at these incoherent boundaries increase significantly due to dislocation pile-up in these alloys [6]. Consequently, interfacial slip and cracking at these internal boundaries accelerate the failure of Mg alloys [7].

For instance, $Mg_{17}Al_{12}$, the crucial intermetallic compound in the Mg-Al-Zn (AZ) system, softens at temperatures above 120℃ [8, 9]. Lattice matching studies [10] have shown that $Mg_{17}Al_{12}$ is incoherent with the α-Mg lattice, suggesting weak bonding at the corresponding phase boundaries. Consequently, the precipitation of large-sized $Mg_{17}Al_{12}$ at grain boundaries makes them highly susceptible to stress concentration, which induces cracking at the grain boundaries during the deformation process [11], particularly at elevated temperatures. The typical room temperature (RT) tensile strength and elongation of the as-cast AZ31 alloy are reported to be 159 MPa and 10%, respectively [12]. Mg-Al-Mn (AM) system exhibits an additional $Al_8Mn_5$ intermetallic compound alongside $Mg_{17}Al_{12}$. However, studies have revealed that mismatches of $(0002)_{Mg}$ // $(30\bar{3}0)_{Al8Mn5}$ and $(0002)_{Mg}$ // $(33\bar{6}0)_{Al8Mn5}$ plane pairs are 17.8% and 19.5%, respectively [13], indicating a similar incoherent relationship between $Al_8Mn_5$ and the Mg matrix [14]. Considering the needle-like morphology of $Al_8Mn_5$, the resulting phase boundaries are more susceptible to cracking compared to those of $Mg_{17}Al_{12}$ [15], and therefore the ductility of the alloy decreases. Typical room temperature tensile strength and elongation to failure of the as-cast AM60 alloy are 172 MPa and 6%, respectively [16]. Ductility deterioration originating from incoherent phase boundaries is also observed in other Mg alloy systems, such as $Mg_2Si$ in the Mg-Al-Si (AS) system [17], and $MgZn/MgZn_2/Mg_2Zn_3$ in the Mg-Zn-Zr (ZK) system [18], etc.

It is now widely accepted that the mechanisms behind classic design criteria and strengthening methods for commercial AZ, AM, ZK, and AS alloys involve introducing more defects (i.e., point, line, plane, and bulk defects) into the alloy, obstructing dislocation motion, and thereby improving the strength [18, 19]. However, most of the introduced boundaries (including grain, sub-grain, and phase boundaries) exhibit incoherent interfacial relationships with the Mg matrix. Consequently, the internal stresses induced by matrix deformation eventually led to the cracking of these weakly bonded boundaries because dislocations cannot be accommodated by incoherent boundaries. This inverse relationship between strength and ductility severely limits the use of Mg alloys in industrial applications [20]. It is worth noting that interfacial matching strengthening has not received sufficient attention, partly because obtaining ultrafine twins in Mg alloys is extremely challenging. Therefore, developing intermetallic compounds that are strongly bonded with the Mg matrix, which enhances simultaneously the strength, ductility, and heat resistance of Mg alloys, while also modulating the inverse relationship between strength and ductility, is currently at the forefront of Mg alloy research.

In fact, lattice-scale interfacial strengthening has yielded considerable success in Cu alloys, Al alloys, and steels. However, coherent boundaries are rarely reported in Mg alloys. For instance, Xu et al. [21] introduced high-density nano twins into pure Cu, resulting in an order of magnitude improvement in the yield strength of Cu (~ 900 MPa) while maintaining good elongation. This approach disrupts the inverse relationship between strength and ductility in metallic materials. Similarly, Song et al. [22] achieved comparable results by introducing $L2_1$-type $Ni_2TiAl$ intermetallic compounds into ferritic steel, generating coherent phase boundaries with the α-Fe matrix within the alloy. This led to a five-fold improvement in creep strength and a doubling of the yield strength, both at 700 ℃ (973 K). The alloy developed by Song et al. [22] is regarded as one of the most optimal ferritic steels in terms of creep resistance. Studies conducted by Jiang et al. [23], Karnesky et al. [24], Ming et al. [25], and Wen et al. [26] have highlighted the significant impact of coherent/semi-coherent internal boundaries (i.e. strongly-bonded boundaries) on enhancing the creep resistance, ductility, and strength of Al alloys and steels.

It is now apparent that developing coherent or semi-coherent boundaries within the alloy is a promising approach for preparing high-strength, high-ductility, lightweight Mg alloys [27]. However, obtaining a large number of coherent boundaries (i.e., twin boundaries (TBs)) within Mg alloys through twinning is almost impossible due to

two main reasons. First, the critical resolved shear stress (CRSS) required for the activation of twinning is much higher than that for slip, making slip more favorable to initiate. Second, twinning in the HCP-structured crystal mainly occurs along the $\{10\bar{1}2\}$ planes at room temperature [28], which implies that the lattice orientation changes after twinning, thus placing the lattice back in an orientation that favors slip. Therefore, twinning in Mg alloys is confined to the early stages where slip is impeded, resulting in a limited number of TBs generated during the process. A feasible method to obtain strongly bonded internal boundaries lies in generating intermetallic compounds that are coherent/semi-coherent with the Mg matrix through alloying. However, there are currently few reports regarding intermetallic compounds that form strong bonds with α-Mg lattice at room temperature [29, 30]. Therefore, in-depth research on the methods to obtain strongly bonded internal boundaries within Mg alloys through alloying, and the mechanisms behind the effects of these boundaries on the strength, ductility, and thermodynamic stability of the alloy, is crucial for exploring future design strategies for Mg alloys [31].

In this work, a novel Mg-Al-Zn-Mn-Y system with a unique $Al_8Mn_4Y$ intermetallic compound is reported, which may be the first intermetallic compound in Mg alloys found to be semi-coherent with the Mg matrix at room temperature. Employing SEM, EDS, XRD, and TEM, the microstructure and phase composition of the alloy are analyzed. Accordingly, the evolution mechanisms of intermetallic compounds within the alloy, and their effects on the solidification of the melt, are elucidated. Subsequently, the interfacial relationship between $Al_8Mn_4Y$ and the Mg matrix is observed, revealing that the newly generated $Al_8Mn_4Y$ is semi-coherent with the α-Mg lattice at phase boundaries. Furthermore, theoretical lattice matching calculations are performed, further verifying their interfacial relationship. Thereafter, the elastic modulus and hardness of $Al_8Mn_4Y$ IMC are obtained using nanoindentation. Its impact on the mechanical properties of Mg alloys at both room and elevated temperatures is explored through tensile tests and fracture analysis. The mechanisms behind this influence are quantified employing four individual contributions, demonstrating that the combination of semi-coherent internal boundaries and granular rare-earth (RE) intermetallic compounds within the alloy provides an ideal solution for developing future high-performance and heat-resistant Mg alloys.

## 2. Sample preparation and experimental methodology

Mg alloy matrix with a composition of Mg-3Al-1Zn-0.4Mn (in wt.%) is prepared using pure Mg, Al, Zn blocks (purity ≥ 99.95%), and Mg-10Mn (wt.%) master alloy. The elemental composition of the prepared Mg alloy matrix is shown in Table 1. Based on the Mg alloy matrix, Mg-Y alloys with Y concentrations of 0.2, 0.4, 0.6, 0.8, and 1.0 wt.% are obtained by adding Mg-30Y (wt.%) master alloy. During the melting process, shielding gas is used with a mixture of $CO_2$ and $SF_6$, with respective flow rates of 2 and 0.05 L/min. The preparation procedure is as follow: Pure Mg blocks are added when the temperature inside the electrical resistance furnace reached 200 ℃. Temperature is then raised to 700 °C and held for 20 min until the Mg blocks are completely melted. Subsequently, Al blocks and Mg-10Mn master alloy are added, and the furnace is further heated up to 750 ℃. Thereafter, the melt is continuously stirred for 2 min after holding for 10 min, followed by slagging, resting, and casting in a metal mold preheated to 200 ℃. This process yielded Mg alloy matrix ingots with diameters of 100 mm. Similarly, in order to obtain Mg-Y alloys, Mg-30Y master alloy is added and the melt is kept at 750 ℃ for another 10 minutes, followed by the same stirring and casting process, as discussed above.

Table 1: Elemental composition of the Mg alloy matrix (wt.%)

| Elements | Al | Zn | Mn | Si | Fe | Cu | Mg |
|---|---|---|---|---|---|---|---|
| wt.% | 3.156 | 1.098 | 0.385 | 0.167 | 0.029 | 0.014 | Balance |

A linear cutting machine is then used to prepare the test specimens, all the specimens are acquired from specific locations on different ingots. Microstructural observations are conducted using optical microscopy (OM, LV150NA, Nikon, Tokyo, Japan) and scanning electron microscopy (SEM, EVO MA 10, ZEISS, Oberkochen, Germany) after inlaying, grinding, polishing, and etching (etching agent: 99 mL deionized $H_2O$, 1 mL $HNO_3$, and

1 g oxalic acid). Elemental and phase composition are determined by employing energy dispersive spectroscopy (EDS, X-Max, Oxford Instruments, Abingdon, UK) and X-ray diffraction (XRD, X'Pert, Malvern Panalytical, Malvern, UK) at a scan speed of 2 °/min. The crystal structures of the IMCs within the alloy are indexed using TEM (Talos F200X, FEI, Hillsboro, OR, USA). Thin sections for use in TEM are prepared using a focused ion beam/SEM (FIB-SEM, Scios, FEI), with an integrated EDS (TEAM, EDAX, Mahwah, NJ, USA). For nanoindentation tests, a Hysitron TI 950 TriboIndenter (Bruker, Billerica, MA, USA) equipped with a Berkovich indenter is used. The load is 10 mN, and the loading, holding, and unloading times are 60, 200, and 20 s, respectively. The nanoindented samples are not etched, as IMCs within the alloy could be easily differentiated based on their colors with the aid of OM. Room and elevated temperature (120°C) tensile tests are conducted on a universal testing machine (CMT-5305GL, Sansi, Shengzhen, China), each test is performed twice, and standard deviations (SD) are calculated. The stretching rate for the tensile tests is 2 mm/min.

The Poisson's ratio required to derive the elastic modulus of the IMC is obtained via first-principle calculations employing the Cambridge Sequential Total Energy Package (CASTEP) code (BIOVIA, San Diego, CA, USA). Before the calculation, the lattice parameters of the unit cell are modified according to the results obtained from TEM. The elastic constants are then calculated with a self-consistent field (SCF) tolerance of $1 \times 10^{-4}$ eV/atom using the Pulay density mixing method. The generalized gradient approximation (GGA) with the Perdew-Burke-Ernzerhof (PBE) functional is used for the exchange-correction functional. An ultrasoft pseudopotential of Vanderbilt type is employed to describe the Coulombic interactions between the valence electrons and ionic core. The calculation of $Al_8Mn_4Y$ in the first irreducible Brillouin zone is performed with a $3 \times 3 \times 2$ k-point mesh using the Monkhorst-Pack scheme, and the cutoff energy of the plane-wave basis is set as 519.70 eV. The tolerances of the calculations of the elastic constants are set as follows: energy within 0.001 eV/cell, maximum force within 100 eV/Å, and maximum displacement within 100 Å. Thus, pseudoatomic calculations are performed for Al $3s^2 3p^1$, Mn $3d^5 4s^2$, and Y $4d^1 6s^2$ [32].

## 3. Experimental results and discussion

### 3.1 Effects of Y on the microstructure and phase composition of Mg alloys

In order to investigate the impact of Y on the Mg-Al-Zn-Mn system, an Mg alloy matrix without Y is prepared in advance as the control group. The microstructure and elemental composition are shown in Figure 1. Clearly, intermetallics within the alloy are primarily distributed along grain boundaries in reticular shapes. However, a small fraction of intermetallics was also observed inside the grains in granular (diameters of approximately 20 μm) or rod-like (lengths of approximately 70 μm) shapes, as seen in Figure 1(b~c). EDS dotting results illustrated in Figure 1(k~l) indicate that the intermetallics at grain boundaries are composed of Mg, Al, and Zn elements, with an atomic ratio close to 7:4:1, while that of the rod-like intermetallics consisting of Al and Mn is 8:5. Combining these findings with the XRD results depicted in Figure 2, it is evident that intermetallics at grain boundaries are the eutectic of $Mg_{17}Al_{12}$ and $MgZn_2$, whereas the rod-like intermetallics are $Al_8Mn_5$. The formation mechanisms and distribution rules behind these IMCs were elaborated in our previous work [33].

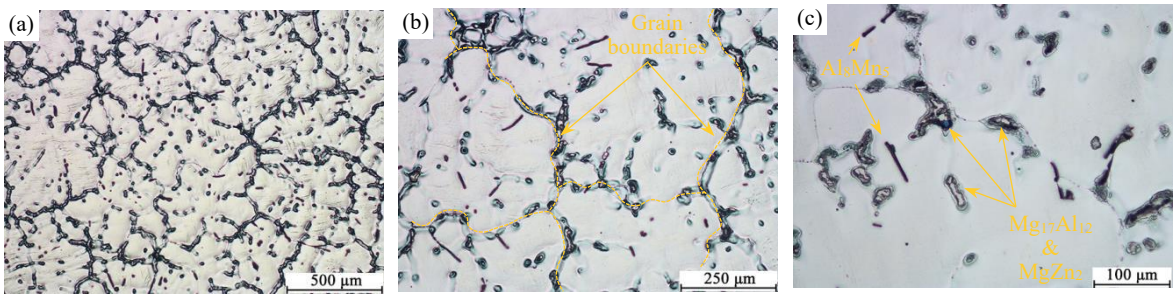

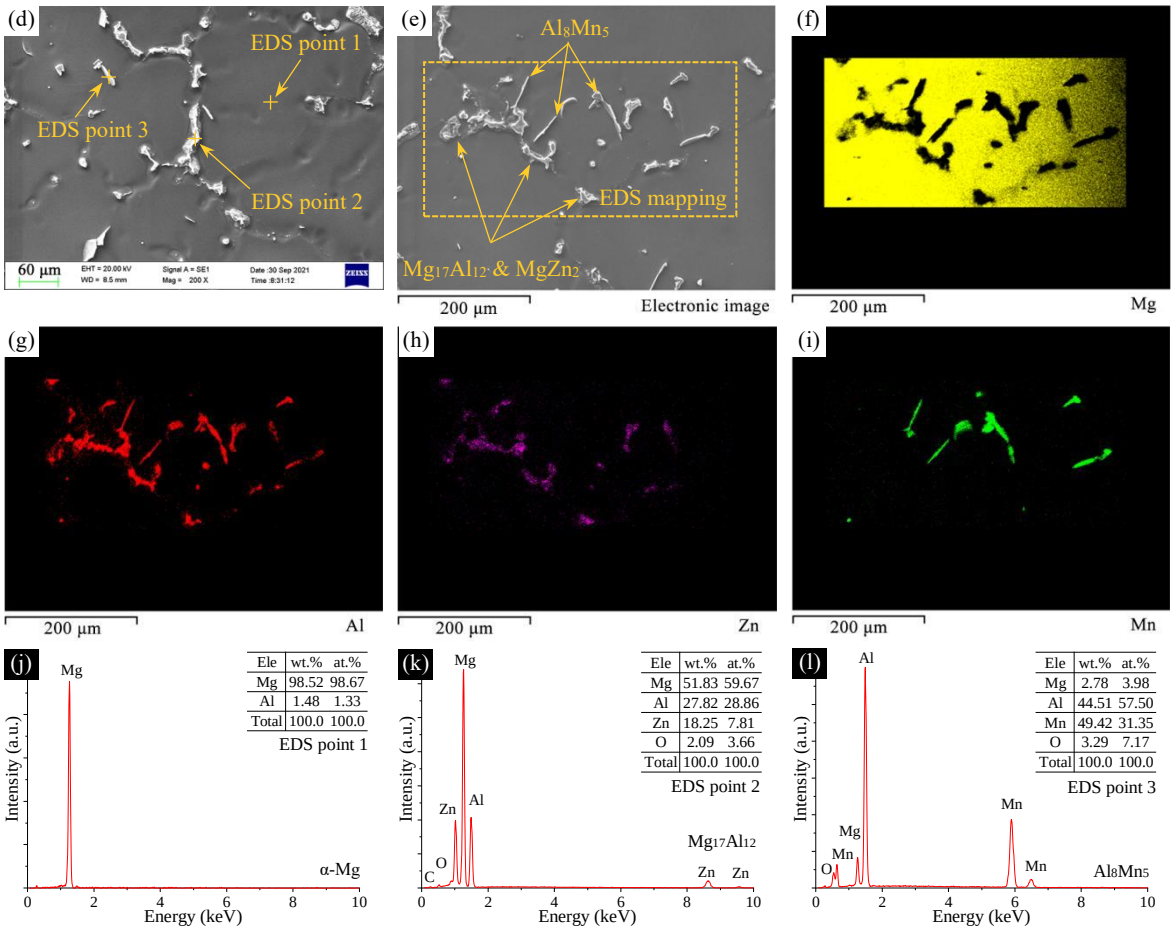


**Figure 1: Microstructure and elemental composition of the Mg alloy matrix. (a, b, c) OM images of the matrix, (d) SEM image of the matrix, (e) EDS mapping position, (f, g, h, i) distributions of Mg/Al/Zn/Mn, (j, k, l) EDS results of α-Mg/$Mg_{17}Al_{12}$/$Al_8Mn_5$.**

XRD results in Figure 2 are consistent with the microstructural observations via SEM and EDS, indicating that the precipitation in the Mg-Al-Zn-Mn system is dominated by the eutectic between Mg and Al elements. In contrast, the XRD analysis of the Mg-Al-Zn-Mn-Y system (Figure 3) reveals the presence of several new intermetallic compounds within the alloy, specifically $Al_8Mn_4Y$ and $Al_2Y$. It is worth noting that the intensity of $Mg_{17}Al_{12}$ in the XRD pattern diminishes upon the addition of Y, suggesting a competition in their formation during the solidification process. This competitive relationship and the underlying mechanisms are also detailed in our previous work [33].

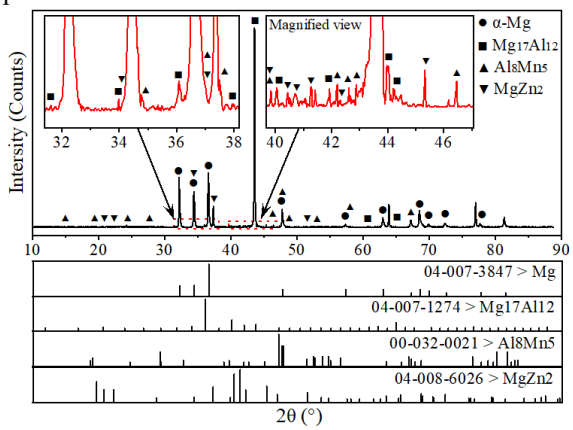


**Figure 2: XRD pattern of the Mg alloy matrix.**

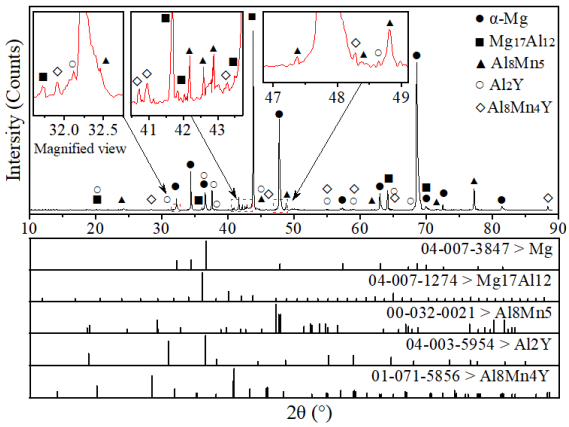


**Figure 3: XRD pattern of the sample containing 0.4 wt.% Y**

The microstructures of the alloys with Y concentrations ranging from 0.2 to 1.0 wt.% are shown in Figure 4. It is evident that the reticulated precipitates at grain boundaries are fragmented into smaller pieces following the addition of Y, and the refinement level increases with higher Y concentrations. The comparison of the microstructures between samples containing 0.2 wt.% and 1 wt.% Y provides robust evidence to support the above deduction, as IMCs within the alloy comprising 1 wt.% Y are transformed entirely into fine particles. It should also be noted that the fraction of granular IMCs consisting of Y increases with increasing Y concentrations, as the number of bright white particles (i.e., IMCs) in the back-scatter electron (BSE) diagrams increases, while the contrast in the BSE diagram corresponds to the atomic number.

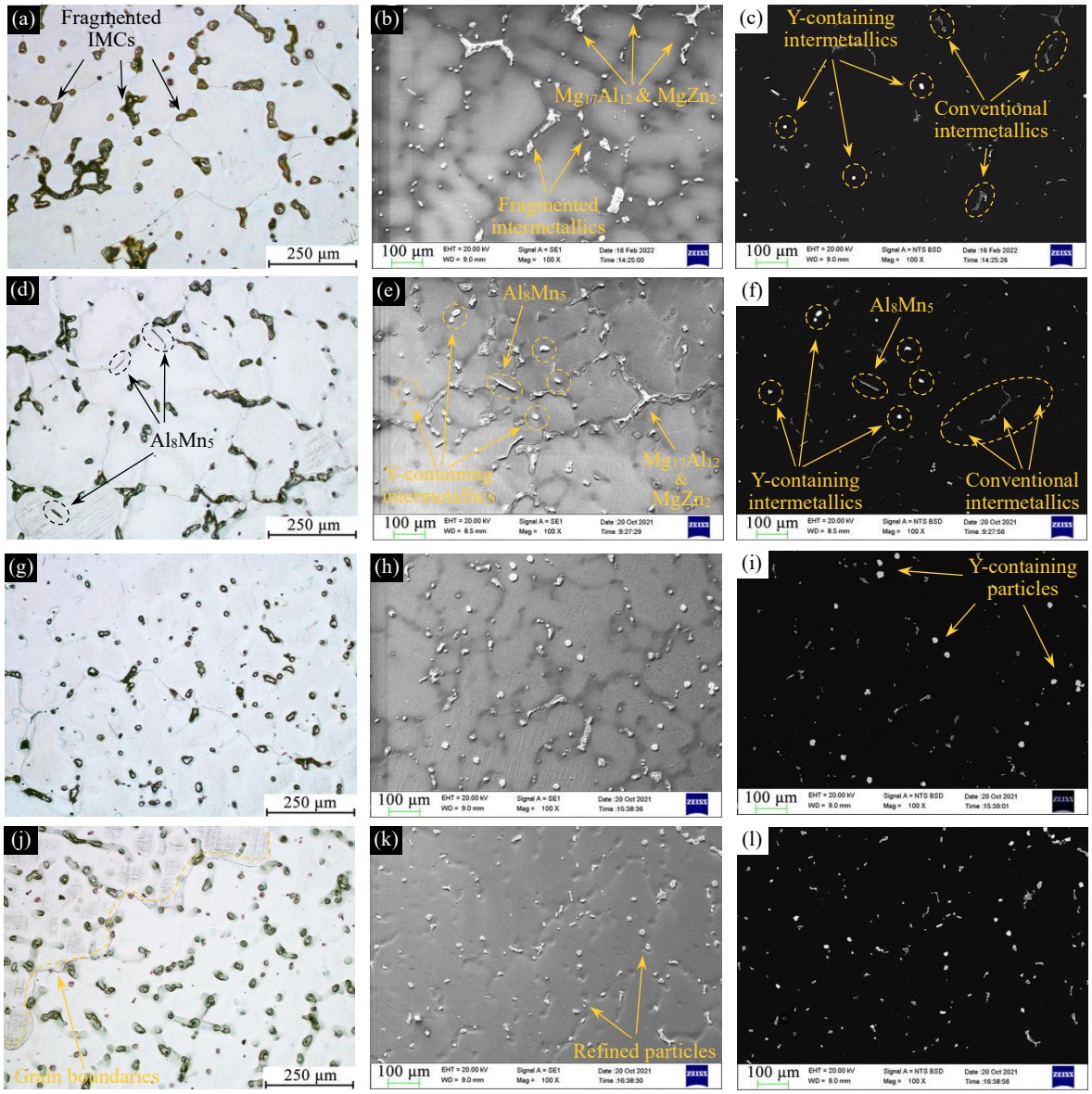


**Figure 4: OM/SEM/BSE images of samples with different Y concentrations. (a, b, c) 0.2 wt.%, (d, e, f) 0.4 wt.%, (g, h, i) 0.6 wt.%, and (j, k, l) 1.0 wt.%.**

EDS mapping and BSE imaging are further employed to identify the distribution rules of intermetallics within the alloy. The results are shown in Figure 5. Both fragmented $Mg_{17}Al_{12}$ and newly generated $Al_8Mn_4Y$ and $Al_2Y$ particles are present within the alloy comprising Y elements. Additionally, Y-containing intermetallics and intermetallics consisting of conventional elements are mixed distributed and randomly dispersed in both grains and at grain boundaries. These distribution patterns are closely related to their respective formation temperatures

and are affected by localized segregation [33]. The underlying mechanisms are detailed in our previous work [33, 34]. It is worth noting that the eutectic points of $Al_8Mn_4Y$ and $Al_2Y$ are higher than that of $Mg_{17}Al_{12}$ [35]. Consequently, the formation of $Al_8Mn_4Y$ and $Al_2Y$ consumes Al solutes in the melt, resulting in a reduction in the proportion of $Mg_{17}Al_{12}$ in the alloy. Accordingly, the total number of IMCs in the alloy decreases as well. The corresponding microstructural evolution with increasing Y concentrations depicted in Figure 4, supports the above discussion.

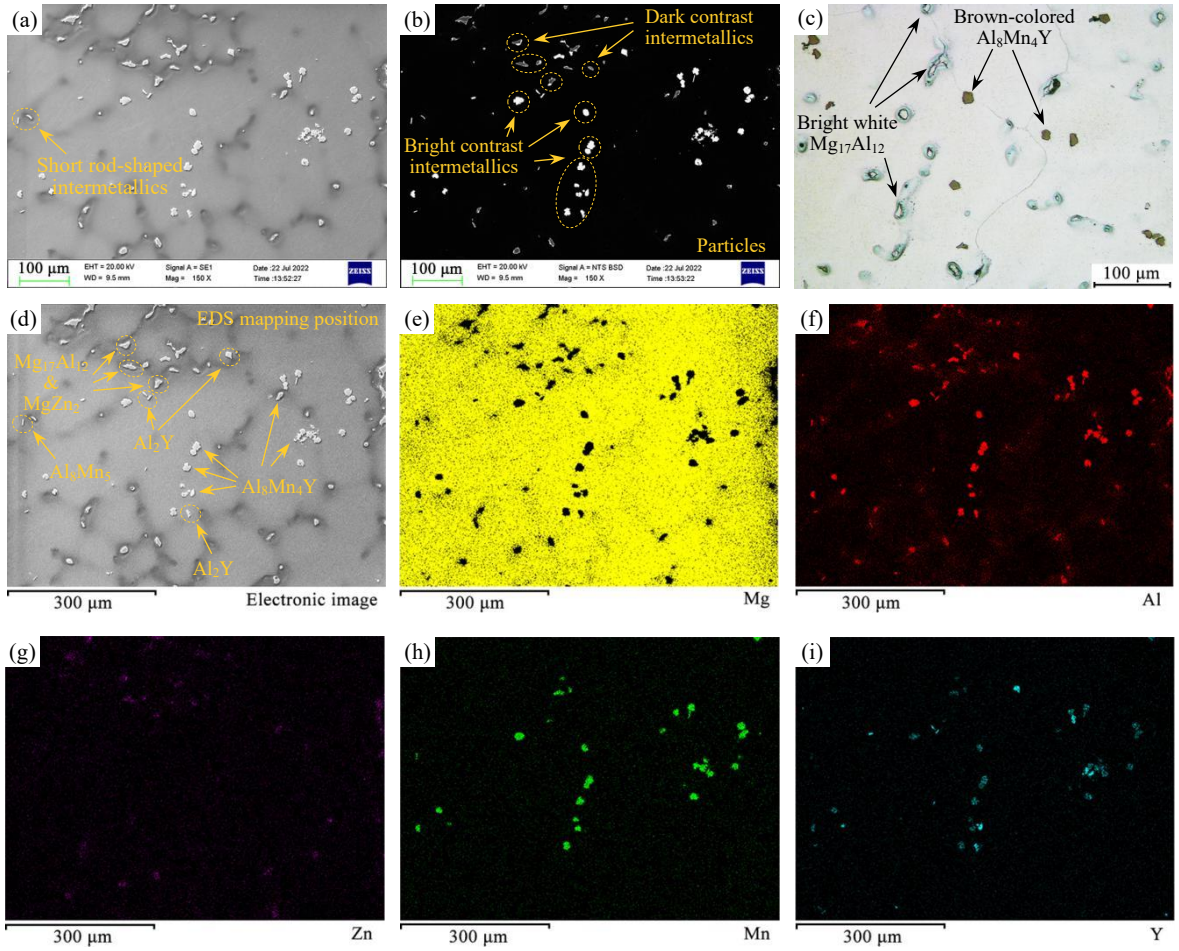


**Figure 5: EDS mapping of the sample containing 1 wt.% Y. (a, b, c) SEM/BSE/OM images of the sample, (d) EDS mapping position, (e, f, g, h, i) distributions of Mg/Al/Zn/Mn/Y elements.**

At this point, the phase composition and distribution rules of IMCs within the Mg-Al-Zn-Mn-Y system have been thoroughly investigated and understood. Figure 6(i~l) exemplifies the typical morphology and elemental composition of intermetallics within the alloy. These intermetallics, including $Al_2Y$, $Al_8Mn_4Y$, $Al_8Mn_5$, and $Mg_{17}Al_{12}$, are highly recognizable due to their unique shapes. Specifically, $Al_2Y$ exhibits a regular rectangular shape (crystal structure: face-centered cubic (FCC)), while $Al_8Mn_4Y$, $Al_8Mn_5$, and $Mg_{17}Al_{12}$ have granular, rod-like, and island-shaped morphologies, respectively.

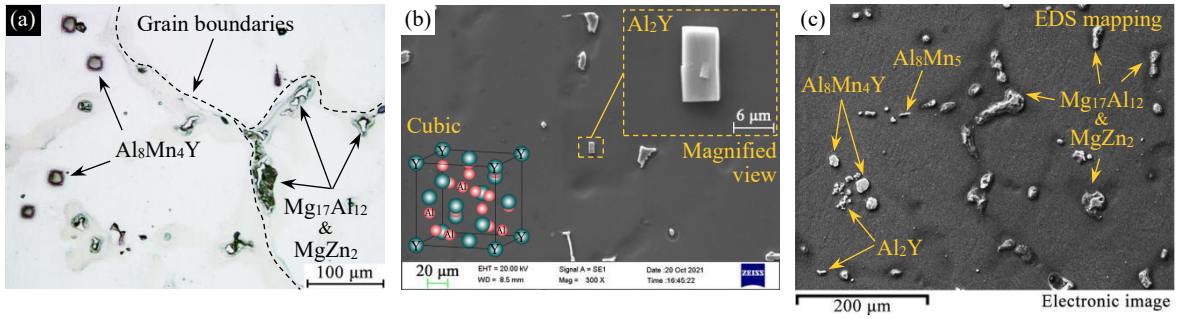

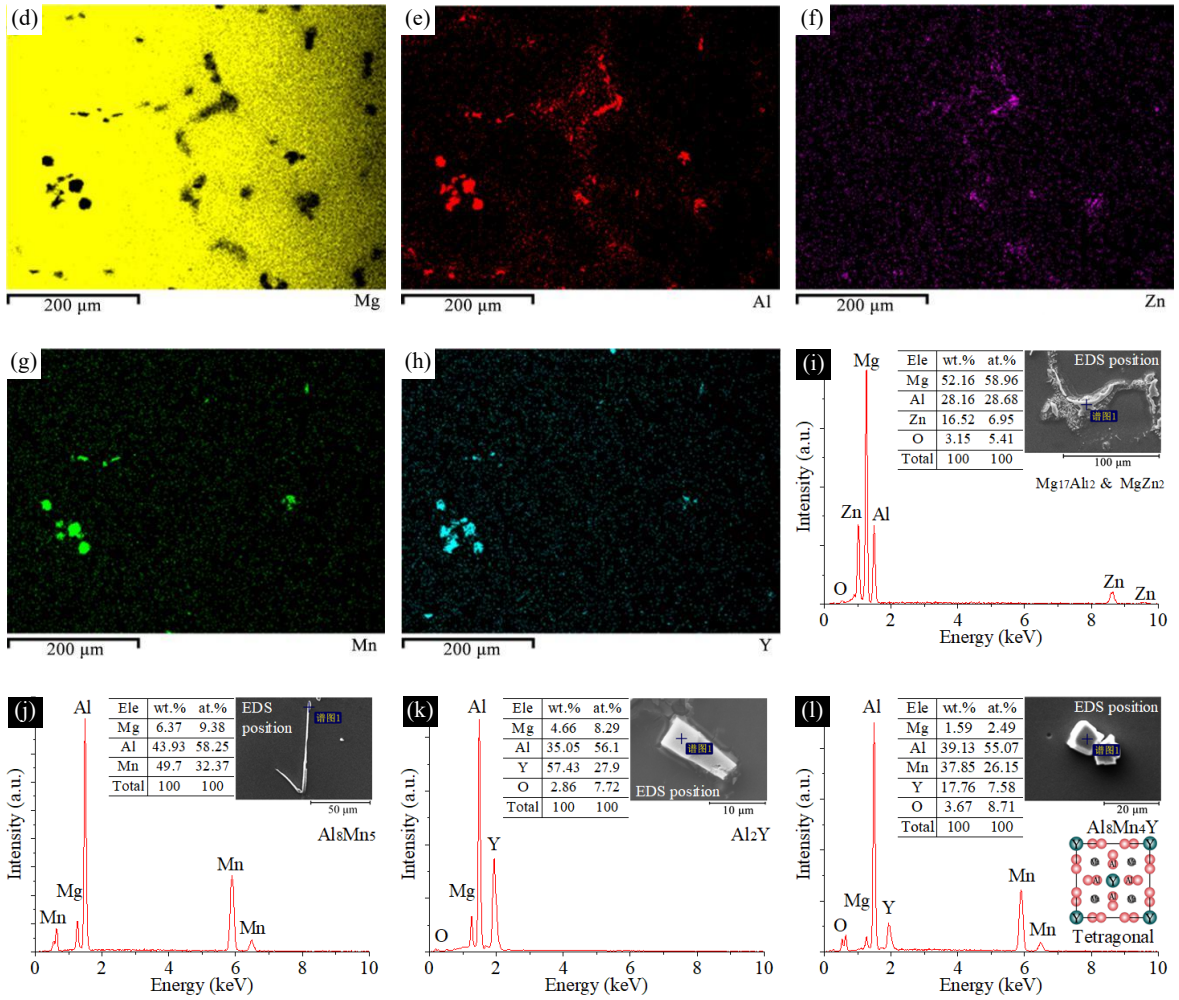


**Figure 6: Identification of the intermetallics in the alloy. (a) OM image of intermetallics in the grains and at the grain boundaries (0.4 wt.% Y), (b) morphology and crystal structure of $Al_2Y$, (c) EDS mapping position, (d~h) distributions of Mg/Al/Zn/Mn/Y, (i~l) EDS results of $Mg_{17}Al_{12}$/$Al_8Mn_5$/$Al_2Y$/$Al_8Mn_4Y$.**

Based on the microstructural and elemental composition results, it can be inferred that the addition of Y refines intermetallic compounds within the Mg-Al-Zn-Mn system. Considering that $Al_8Mn_4Y$ and $Al_2Y$ particles are also generated in the alloy, it is evident that an appropriate quantity of Y not only modifies the composition of intermetallics within the alloy but also optimizes their morphologies. This results in a reinforced structure where newly generated Y-containing particles (i.e., $Al_8Mn_4Y$ and $Al_2Y$) are mixed with the modified intermetallics consisting of conventional elements. It is well accepted that the formation of smaller-sized particles in the alloy benefits the improvement of strength and ductility, as fine particles reduce stress concentration at phase boundaries during deformation. However, from the perspective of alloy microstructure and combining the microstructural observation results in Figures 4~6, it is apparent that excessive Y concentration destroys the desired proportion of Y-containing intermetallics and conventional intermetallics in the reinforced structure. Therefore, a low level of Y addition is recommended in the Mg-Al-Zn-Mn system.

## 3.2 Structure of $Al_8Mn_4Y$ intermetallic compound

$Al_8Mn_4Y$ is rarely reported in previous studies [27, 36], and literature regarding the Al-Mn-Y ternary phase diagram is limited [37]. In fact, $Al_8Mn_4Y$ (Figure 7) crystallizes in a tetragonal I4/mmm space group featuring $a = b \neq c$ and $\alpha = \beta = \gamma = 90°$, with lattice parameters of $a = b = 8.856$ Å and $c = 5.112$ Å. It is worth noting that experimental characterization of $Al_8Mn_4Y$ is currently lacking. However, microstructural observations have revealed that $Al_8Mn_4Y$ significantly refines IMCs in the Mg-Al-Zn-Mn system and forms a reinforced structure

within this system. Therefore, gaining a deeper understanding of the role of $Al_8Mn_4Y$ in Mg alloys is necessary.

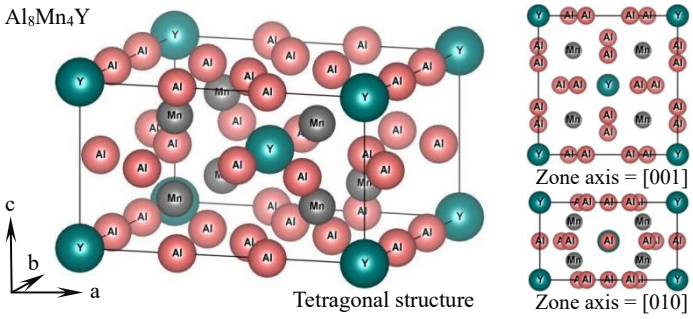


**Figure 7: Crystal structure of $Al_8Mn_4Y$ intermetallic compound.**

TEM is utilized to investigate the crystal structure of $Al_8Mn_4Y$. A thin section with a thickness of approximately 4 μm (Fig. 8(d)) is prepared in advance from the sample containing 0.8 wt.% Y using FIB-SEM. The preparation process is shown in Figure 8(a~e). Before FIB cutting, EDS is employed to confirm the elemental composition of the target, and the results are illustrated in Figure 8(f). EDS spectra suggest that the atomic ratio of Al, Mn, and Y in the target is approximately 8:4:1, confirming that the target is the desired $Al_8Mn_4Y$.

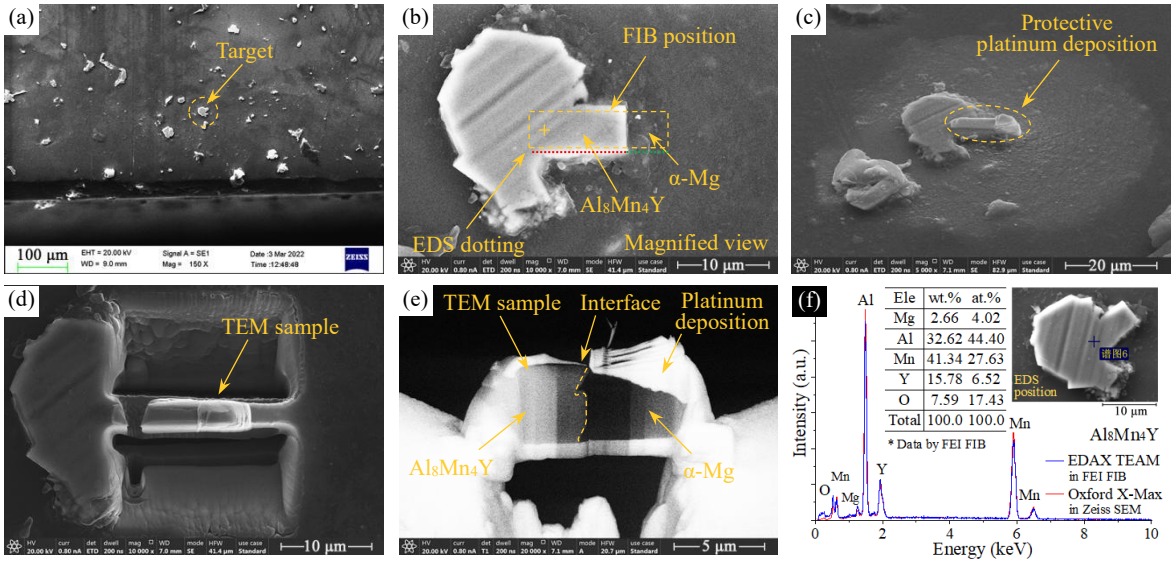


**Figure 8: Preparation of the thin-section via FIB-SEM. (a) SEM image of the target in the sample containing 0.8 wt.% Y, (b) FIB cutting position, (c) protective Pt deposition, (d) prepared thin-section for use in TEM, (e) cross-sectional morphology of the thin-section, (f) EDS dotting results of the target captured using Oxford and EDAX EDS.**

Typical bright-field (BF) image of the thin-section is illustrated in Figure 9(a). With the help of EDS (Figure 9(d)) and Z-contrast, $Al_8Mn_4Y$ and α-Mg regions are easily differentiated. Accordingly, selected area electron diffraction (SAED) was performed, and the resulting diffraction patterns are shown in Figure 9(b, e).

Calibration of the diffraction patterns reveals that the zone axis is <100> for the $Al_8Mn_4Y$ region and $<2\bar{1}\bar{1}0>$ (equivalent to <100> in Miller indices) for the α-Mg region. Theoretical diffraction patterns (Figure 9(c) and Figure 9(f)) calculated based on these results are highly consistent with those obtained from SAED experiments. Consequently, the detailed orientations of $Al_8Mn_4Y$ and α-Mg unit cells are deduced, as shown in the lower left of Figure 9(c) and Figure 9(f).

Measurements of the experimental diffraction pattern ($Al_8Mn_4Y$) indicate that the interplanar spacings of {020} and {011} planes are $d_{\{020\}} = 2.24\ nm^{-1}$ and $d_{\{011\}} = 2.26\ nm^{-1}$, respectively. Accordingly, the lattice parameters $a$ and $b$ are calculated: $a = b = d_{\{010\}} = d_{\{020\}} / 2 = 1.12\ nm^{-1} = 8.929$ Å. Subsequently, the lattice parameter $c$ is obtained: $d_{\{011\}} = 2.26\ nm^{-1} = 4.425$ Å and $c = d_{\{011\}} / cos\theta = 5.095$ Å, where $\theta$ is the angle between the {011} and {001} planes, and $cos\theta$ is determined using $sin\theta = d_{(011)} / b$. It is worth noting that the lattice parameters obtained

in this work agree with those in the standard powder diffraction file (PDF, Card No: 00-033-0030) provided by the International Centre for Diffraction Data (ICDD), with values $a = b = 8.856$ Å and $c = 5.112$ Å. This provides clear evidence of accurately calibrating $Al_8Mn_4Y$ using experimental methods.

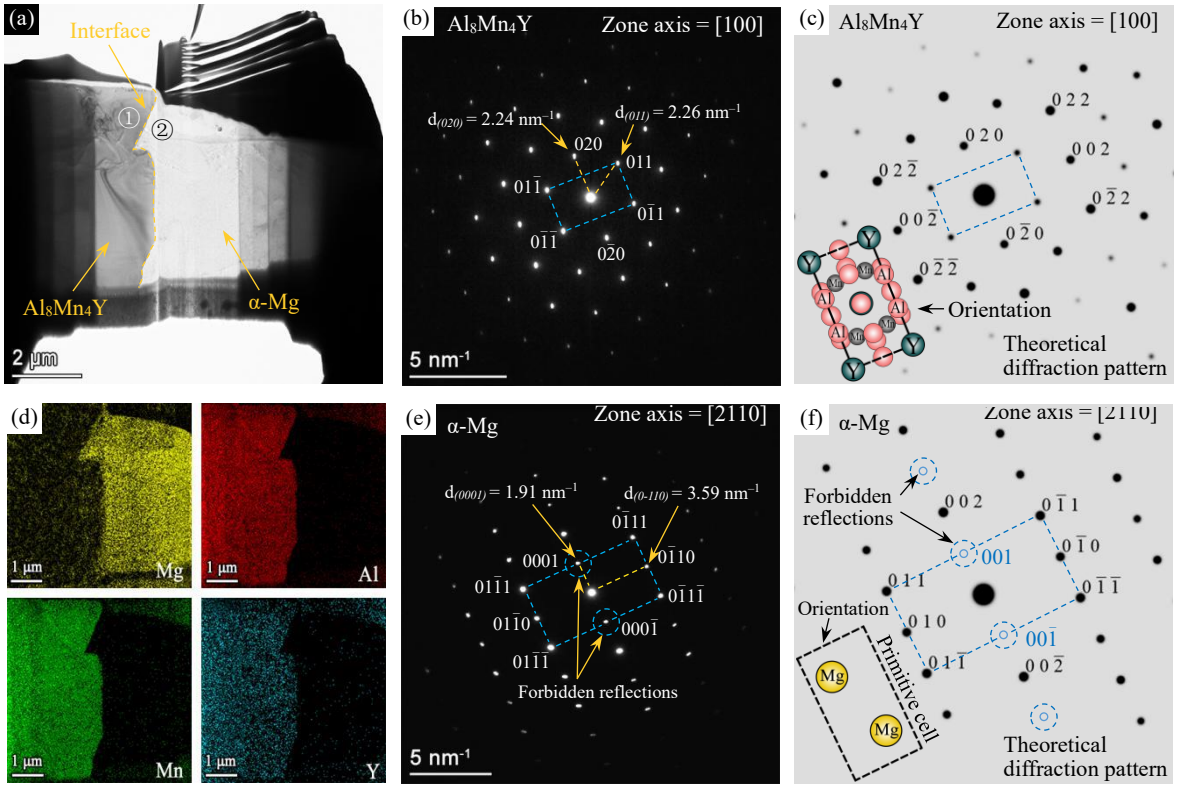


**Figure 9: TEM results of α-Mg and $Al_8Mn_4Y$. (a) BF image of the sample, (b) SAED pattern of $Al_8Mn_4Y$, (c) theoretical diffraction pattern of $Al_8Mn_4Y$ along [100] zone axis, (d) EDS mapping results of the thin-section, (e) SAED pattern of α-Mg, (f) theoretical diffraction pattern of α-Mg along $[2\bar{1}\bar{1}0]$ zone axis.**

Figure 9(e) and Figure 9(f) present the experimental and theoretical diffraction patterns of α-Mg. It is noteworthy that, the reflections corresponding to {0001} and $\{000\bar{1}\}$ planes in the experimental diffraction pattern appear less intense compared to the surrounding reflections. This phenomenon is attributed to the electron diffraction extinction effect. The observed dimming of certain reflections indicate that the thin section prepared is slightly thicker, leading to secondary diffraction contributing to the re-emergence of the extinction spots.

Similarly, the diffraction pattern of α-Mg is measured, revealing the interplanar spacings of {0001} and $\{0\bar{1}10\}$ planes to be $d_{\{0001\}} = 1.91$ nm$^{-1}$ = 5.236 Å and $d_{\{0-110\}} = 3.59$ nm$^{-1}$ = 2.786 Å, respectively. These values indicate that the lattice parameter $c = d_{\{0001\}} = 5.236$ Å. Considering that the angle between $\{0\bar{1}10\}$ and $\{10\bar{1}0\}$ planes measures 60°, the lattice parameters $a$ and $b$ are determined as follows: $a = b = d_{(0-110)} / sin60° = 3.216$ Å. These results are highly consistent with those in the standard PDF (Card No: 00-35-0821), which reports the lattice parameters of α-Mg as $a = b = 3.209$ Å and $c = 5.211$ Å.

HRTEM and SAED serve the same role in analyzing the lattice parameters. However, HRTEM utilizes phase contrast, providing a comprehensive map of lattice for the entire view field. This characteristic makes HRTEM useful in exploring lattice orientation and defects in the alloy. Direct measurements of the HRTEM images reveal that the interplanar spacings of {020} and {011} planes are $d_{\{020\}} = 4.462$ Å and $d_{\{011\}} = 4.430$ Å, respectively, indicating the lattice parameters of $Al_8Mn_4Y$ to be $a = b = 8.924$ Å and $c = 5.103$ Å. Similarly, the lattice parameters of α-Mg are determined based on the interplanar spacings of $d_{\{0-110\}} = 2.789$ Å and $d_{\{0001\}} = 5.229$ Å, suggesting lattice parameters of $a = b = 3.221$ Å and $c = 5.229$ Å, as annotated in Figure 10(b, c). These results derived from HRTEM are highly consistent with those obtained from the SAED patterns.

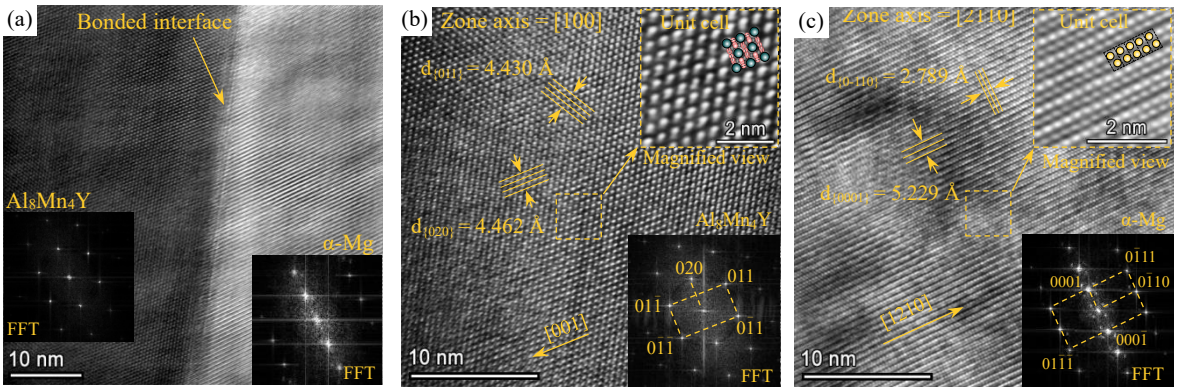


**Figure 10: HRTEM images. (a) the bonding interface, (b~c) HRTEM images of $Al_8Mn_4Y$ and α-Mg.**

It is worth noting that the lattices of both $Al_8Mn_4Y$ and α-Mg in the HRTEM images are arranged, with minimal defects observed, as depicted in Figure 10(a~c). Interestingly, the orientations of the lattices on both sides of the contact interface (i.e., the phase boundary between $Al_8Mn_4Y$ and α-Mg) appear to be aligned. The magnified views of the HRTEM images and the detailed orientations of the $Al_8Mn_4Y$ and α-Mg unit cells deduced (shown in the upper right of Figure 10(b, c)), strongly support the interfacial relationship proposed above.

## 3.3 Crystallographic orientation relationship between α-Mg and $Al_8Mn_4Y$

Magnified HRTEM observations and SAED analysis are further performed on the bonding interface between α-Mg and $Al_8Mn_4Y$. The results showed that the lattice fringes on both sides are regularly matched at the phase boundary, demonstrating the quasi-parallel relationship between $\{010\}_{Al8Mn4Y}$ and $\{0001\}_{\alpha\text{-}Mg}$ planes, as indicated by the lines in Figure 10(a) and Figure 12. Measurements of the bonding interface through the SAED method reveal that the angle between $\{0\bar{1}0\}_{Al8Mn4Y}$ and $\{000\bar{1}\}_{\alpha\text{-}Mg}$ planes is only 3.9° (Figure 11(c)), further verifying the excellent interfacial matching between the lattices of $Al_8Mn_4Y$ and α-Mg. Given that the $\gamma$ angles of both $Al_8Mn_4Y$ and α-Mg unit cells are 90°, the bonding between the $Al_8Mn_4Y$ intermetallic compound and the Mg matrix occurs through the $\{001\}_{Al8Mn4Y}$ and $\{0\bar{1}10\}_{\alpha\text{-}Mg}$ plane pair, which is perpendicular to the quasi-parallel planes of $\{0\bar{1}0\}_{Al8Mn4Y}$ // $\{000\bar{1}\}_{\alpha\text{-}Mg}$.

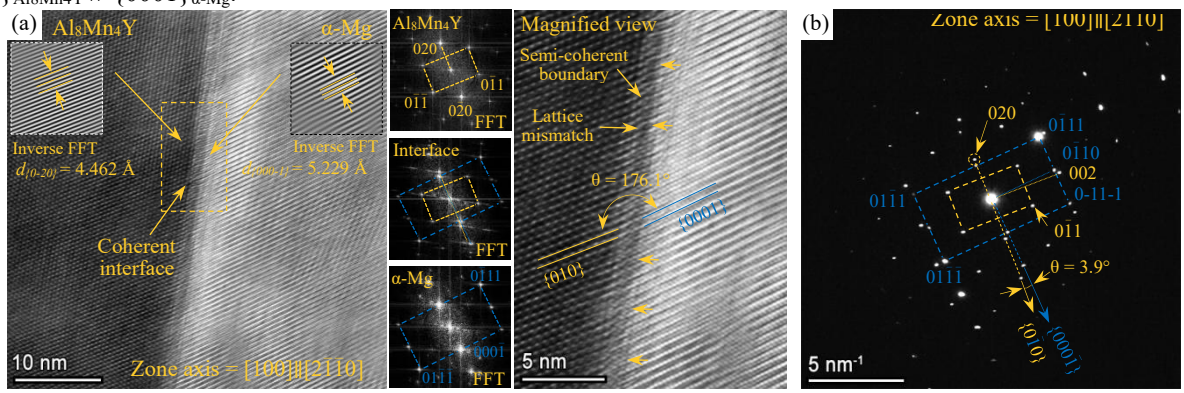


**Figure 11: Crystallographic orientation relationship between the $(000\bar{1})_{\alpha\text{-}Mg}$ and the $(01\bar{1})_{Al8Mn4Y}$ planes. (a) HRTEM image, (b) SAED pattern of the bonding interface.**

In fact, α-Mg and $Al_8Mn_4Y$ share many similar lattice characteristics, such as both having $\gamma$ angles of 90° and lattice parameters $a = b$. Interestingly, the $c$ values of α-Mg and $Al_8Mn_4Y$ are close, measuring 5.211 Å and 5.112 Å, respectively, while the $a$ and $b$ values of the $Al_8Mn_4Y$ unit cell are approximately three times those of α-Mg. These features indicate that $Al_8Mn_4Y$ and α-Mg have the potential to form a semi-coherent phase boundary.

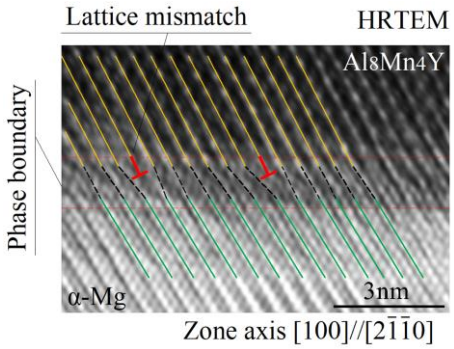


**Figure 12: The magnified observation of the bonding interface between $Al_8Mn_4Y$ and α-Mg.**

It is worth noting that typical lattice mismatches are observed every four $Al_8Mn_4Y$ lattices along the $<010>_{Al8Mn4Y}$ direction at the bonding interface, as annotated in Figure 12. This finding suggests that $Al_8Mn_4Y$ exhibits a semi-coherent relationship with the α-Mg lattice along the $[100]_{Al8Mn4Y}$ // $[2\bar{1}\bar{1}0]_{\alpha\text{-}Mg}$ zone axis, with bonding achieved via the $\{001\}_{Al8Mn4Y}$ and $\{0\bar{1}10\}_{\alpha\text{-}Mg}$ plane pair. Additionally, since $Al_8Mn_4Y$ intermetallic compounds exhibit granular shapes, bonding between $Al_8Mn_4Y$ and α-Mg lattices may also occur through other plane pairs at distinct positions, assuming that fine $Al_8Mn_4Y$ particles are long-range ordered.

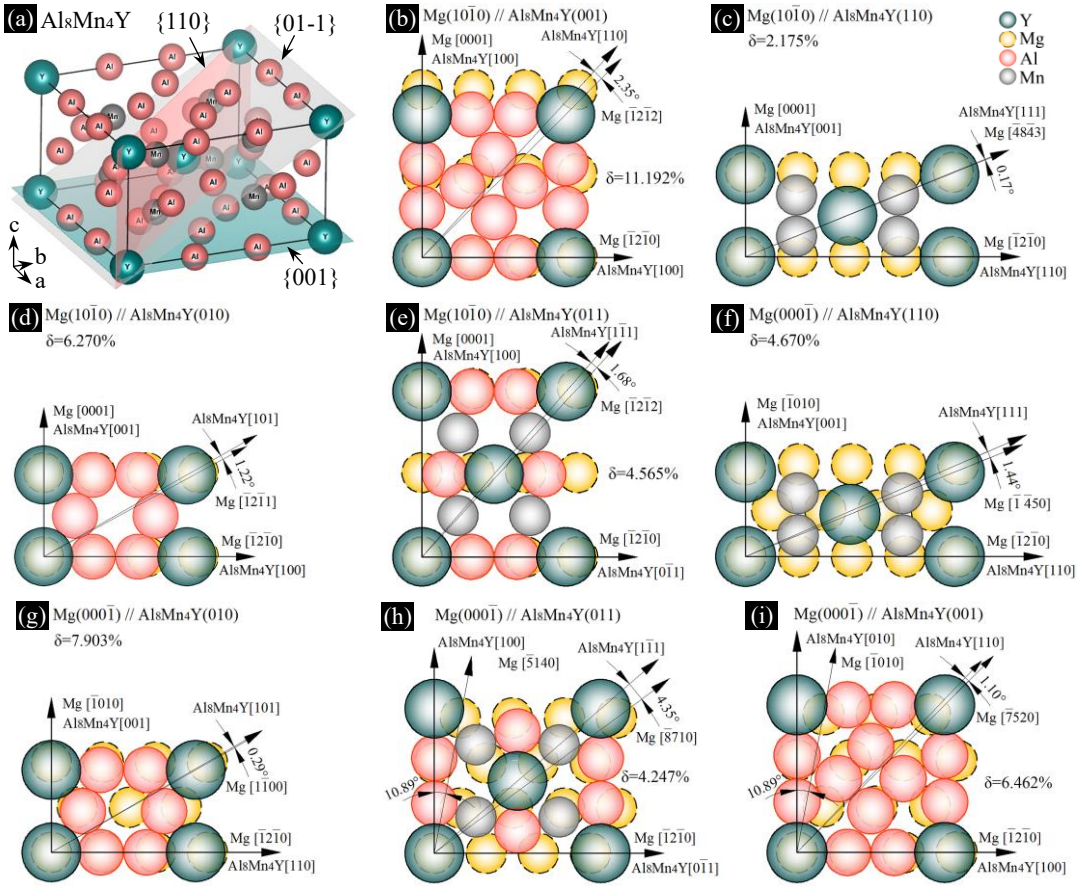


**Figure 13: Crystallographic matching relationships between plane pairs in α-Mg and $Al_8Mn_4Y$ unit cells. (a) $Al_8Mn_4Y$ unit cell, (b) (10$\bar{1}$0)//(001), (c) (10$\bar{1}$0)//(110), (d) (10$\bar{1}$0)//(010), (e) (10$\bar{1}$0)//(011), (f) (000$\bar{1}$)//(110), (g) (000$\bar{1}$)//(010), (h) (000$\bar{1}$)//(011), and (i) (000$\bar{1}$)//(001).**

The matching between $Al_8Mn_4Y$ and α-Mg unit cells is theoretically evaluated using mismatch theory [38]. The approach is expressed in Equation 1, where $\delta$ is the lattice mismatch, $(hkl)_{Mg}$ and $(hkl)_P$ are the respective low-index planes in α-Mg and $Al_8Mn_4Y$ unit cells, $[hkl]^i_{Mg}$ and $[hkl]^i_P$ are the low-index orientations in $(hkl)_{Mg}$ and $(hkl)_P$ planes, $d^i_{(hkl)Mg}$ is the interatomic spacing along the $[hkl]^i_{Mg}$ orientation, and $\theta$ is the angle between $[hkl]^i_{Mg}$ and $[hkl]^i_P$ orientations.

$$\delta_{(hkl)_P}^{(hkl)_{Mg}} = \sum_{i=1}^{3} \frac{\left| (d^i_{[uvw]_{Mg}} \times \cos\theta) - d^i_{[uvw]_P} \right|}{d^i_{[uvw]_P}} \times \frac{1}{3} \times 100\% \quad \cdots\cdots\cdots\cdots\cdots\cdots\cdots\cdots\cdots\cdots \quad 1$$

$Al_8Mn_4Y$ exhibits a tetragonal structure with high symmetry. It is important to note that only four types of low-index planes are observed within its unit cell, namely (100), (001), (011), and (110) planes. Similarly, α-Mg also possesses high symmetry, featuring two types of low-index planes within its unit cell: the $(10\bar{1}0)$ prismatic plane and the (0001) basal plane ($(10\bar{1}0)$, $(01\bar{1}0)$, and $(1\bar{1}00)$ planes are equivalent due to symmetry). As a result, the combinations of low-index planes within $Al_8Mn_4Y$ and α-Mg unit cells are limited, totaling only 8. These specific combinations and their corresponding mismatches are elaborated in Figure 13 and Table 2.

Theoretical calculations reveal several plane pairs with interfacial mismatches below 5%, including $(110)_{Al8Mn4Y}$ // $(10\bar{1}0)_{\alpha\text{-}Mg}$, $(011)_{Al8Mn4Y}$ // $(10\bar{1}0)_{\alpha\text{-}Mg}$, $(110)_{Al8Mn4Y}$ // $(0001)_{\alpha\text{-}Mg}$, and $(011)_{Al8Mn4Y}$ // $(0001)_{\alpha\text{-}Mg}$. Among these, the $(110)_{Al8Mn4Y}$ // $(10\bar{1}0)_{\alpha\text{-}Mg}$ plane pair exhibits the lowest mismatch of only 2.175%, signifying an excellent semi-coherent relationship between the $Al_8Mn_4Y$ and α-Mg unit cells. Additionally, other plane pairs, such as $(100)_{Al8Mn4Y}$ // $(10\bar{1}0)_{\alpha\text{-}Mg}$, $(001)_{Al8Mn4Y}$ // $(10\bar{1}0)_{\alpha\text{-}Mg}$, $(100)_{Al8Mn4Y}$ // $(0001)_{\alpha\text{-}Mg}$, and $(001)_{Al8Mn4Y}$ // $(0001)_{\alpha\text{-}Mg}$, display mismatches in the range of 5% to 12%, further demonstrating the favorable matching between these two lattices.

**Table 2: Lattice matching between planes in α-Mg and $Al_8Mn_4Y$ unit cells**

| **Crystal Planes** | **Mg($10\bar{1}0$) // $Al_8Mn_4Y$(110)** | | | **Mg($10\bar{1}0$) // $Al_8Mn_4Y$(011)** | | | **Mg($10\bar{1}0$) // $Al_8Mn_4Y$(100)** | | |
|---|---|---|---|---|---|---|---|---|---|
| Mg [*hkil*] | [0001] | [$\bar{4}\bar{8}43$] | [$\bar{1}2\bar{1}0$] | [0001] | [$\bar{1}2\bar{1}2$] | [$\bar{1}2\bar{1}0$] | [0001] | [$\bar{1}2\bar{1}1$] | [$\bar{1}2\bar{1}0$] |
| $Al_8Mn_4Y$ [*hkl*] | [001] | [111] | 110 | [100] | [1$\bar{1}$1] | [0$\bar{1}$1] | [001] | [101] | [100] |
| $d_{\alpha\text{-}Mg}$ (Å) | 5.236 | 13.617 | 12.864 | 10.472 | 14.239 | 9.648 | 5.236 | 10.977 | 9.648 |
| $d_{Al8Mn4Y}$ (Å) | 5.095 | 13.889 | 12.628 | 10.280 | 13.617 | 8.929 | 5.095 | 10.028 | 8.929 |
| $\theta$ (°) | 0.000 | 0.170 | 0.000 | 0.000 | 1.680 | 0.000 | 0.000 | 1.220 | 0.000 |
| $\delta_{linear}$ (%) | 2.693% | 1.997% | 1.835% | 1.833% | 4.409% | 7.452% | 2.693% | 8.666% | 7.452% |
| $\delta_{facial}$ (%) | | 2.175% | | | 4.565% | | | 6.270% | |

| **Crystal Planes** | **Mg($10\bar{1}0$) // $Al_8Mn_4Y$(001)** | | | **Mg(0001) // $Al_8Mn_4Y$(110)** | | | **Mg(0001) // $Al_8Mn_4Y$(011)** | | |
|---|---|---|---|---|---|---|---|---|---|
| Mg [*hkil*] | [0001] | [$\bar{1}2\bar{1}2$] | [$\bar{1}2\bar{1}0$] | [$\bar{1}$010] | [$\bar{1}\bar{4}$50] | [$\bar{1}2\bar{1}0$] | [$\bar{1}$010] | [$\bar{8}$710] | [$\bar{1}2\bar{1}0$] |
| $Al_8Mn_4Y$ [*hkl*] | [100] | [110] | [100] | [001] | [111] | [110] | [100] | [1$\bar{1}$1] | [0$\bar{1}$1] |
| $d_{\alpha\text{-}Mg}$ (Å) | 10.472 | 14.239 | 9.648 | 5.570 | 14.018 | 12.964 | 8.509 | 14.018 | 9.648 |
| $d_{Al8Mn4Y}$ (Å) | 8.929 | 12.628 | 8.929 | 5.095 | 13.617 | 12.628 | 8.929 | 13.617 | 10.280 |
| $\theta$ (°) | 0.000 | 2.350 | 0.000 | 0.000 | 1.440 | 0.000 | 10.890 | 4.390 | 0.000 |
| $\delta_{linear}$ (%) | 14.735% | 11.389% | 7.452% | 8.528% | 2.891% | 2.592% | 3.046% | 3.146% | 6.551% |
| $\delta_{facial}$ (%) | | 11.192% | | | 4.670% | | | 4.247% | |

| **Crystal Planes** | **Mg(0001) // $Al_8Mn_4Y$(100)** | | | **Mg(0001) // $Al_8Mn_4Y$(001)** | | |
|---|---|---|---|---|---|---|
| Mg [*hkil*] | [$\bar{1}$010] | [$\bar{1}$100] | [$\bar{1}2\bar{1}0$] | [$\bar{1}$010] | [$\bar{7}$520] | [$\bar{1}2\bar{1}0$] |
| $Al_8Mn_4Y$ [*hkl*] | [001] | [101] | [110] | [010] | [110] | [100] |
| $d_{\alpha\text{-}Mg}$ (Å) | 5.570 | 11.141 | 9.648 | 8.509 | 11.595 | 9.648 |
| $d_{Al8Mn4Y}$ (Å) | 5.095 | 10.280 | 8.929 | 8.929 | 12.628 | 8.929 |
| $\theta$ (°) | 0.000 | 0.290 | 0.000 | 10.890 | 1.100 | 0.000 |
| $\delta_{linear}$ (%) | 8.528% | 7.729% | 7.452% | 3.046% | 8.889% | 7.452% |
| $\delta_{facial}$ (%) | | 7.903% | | | 6.462% | |

Reports by Doi [39] regarding the relationship between lattice mismatch and the morphology of intermetallic compounds reveal that intermetallics precipitate spherically in the alloy when their mismatch with the matrix is <

3%. However, they adopt a disc-shaped morphology when the mismatch is between 3% and 5%. These findings shed light on the predominant granular shape of $Al_8Mn_4Y$ precipitation, as illustrated in Figure 5 and Figure 6.

Indeed, the formation of coherent/semi-coherent interfaces between unit cells with different crystal structures is challenging. Therefore, few intermetallic compounds are reported coherent or semi-coherent with the α-Mg lattice at room temperature in previous Mg research [40, 41]. Gao et al.[40] conducted studies revealing that $Mg_3Gd$, a transitional phase that forms during aging, demonstrates semi-coherence with the Mg matrix. Notably, the alloy achieves its maximum hardness (104 HV) upon the formation of $Mg_3Gd$ and the corresponding semi-coherent boundaries within the alloy. However, $Mg_3Gd$ is metastable, and the semi-coherence is immediately lost as the phase transformations proceed: β"($Mg_3Gd$) → β'($Mg_{(3-5)}Gd$) → β1($Mg_{(3-5)}Gd$) → β($Mg_5Gd$). Consequently, the strengthening effect originating from semi-coherent boundaries is no longer observed. Nishijima et al.[41] also reported an intermetallic compound ($Mg_7Y$) that is coherent with α-Mg lattice. Similarly, $Mg_7Y$ transforms into $Mg_{24}Y_5$ through α-Mg → β" (GP zones) → β' ($Mg_7Y$) → β ($3Mg_{24}Y_5$) during aging. Evidently, maintaining coherence between intermetallics and the Mg matrix is challenging due to the susceptibility of the crystal structures of metastable intermetallics to alterations during thermal cycling. Therefore, the preservation of coherence highly relies on thermal stability. Notably, it is crucial to highlight that rare earth intermetallics possess exceptional thermal stability. Experimental findings have revealed that $Al_8Mn_4Y$ remains stable and maintains a high concentration within the alloys solidified under normal cooling rates. These observations serve as compelling evidence, affirming the absence of any phase transition for $Al_8Mn_4Y$ during the solidification process from 750°C to room temperature. Further insights into the evolution of phases within the Mg-Al-Zn-Mn-Y system during solidification can be found in our earlier work [33]. This specific attribute contributes to the persistent presence of coherent/semi-coherent boundaries between $Al_8Mn_4Y$ and the Mg matrix, sustaining this relationship until room temperature.

In the above, we presented the semi-coherent relationship between $Al_8Mn_4Y$ and α-Mg lattices through theoretical and experimental investigation. This establishes $Al_8Mn_4Y$ as the first reported intermetallic compound in Mg alloys that demonstrates semi-coherence with the α-Mg lattice at room temperature. It is fascinating that the lattices on both sides of the coherent/semi-coherent boundaries are well-matched, facilitating the accommodation of dislocations and enabling their penetration across the phase boundaries. Intriguingly, these mechanisms reduce stress concentrations at the phase boundaries, significantly alleviating cracking during the deformation of the alloy [42]. It is important to note that coherent / semi-coherent boundaries possess low interfacial energy and nucleation barriers, promoting the uniform precipitation of these intermetallics within the alloy. Furthermore, the resulting phase boundaries are highly thermally stable at elevated temperatures. As a result, the strength, ductility, and heat resistance of the alloy are simultaneously enhanced. Studies [24, 43] have shown that intermetallic compounds, which exhibit coherent/semi-coherence with the matrix, play a superior role in improving the comprehensive mechanical properties of the alloy compared to the Laves phase. These mechanical properties are investigated in the following.

## 3.4 Tensile test and fracture analysis of the alloy

To validate the strengthening effect of $Al_8Mn_4Y$ in Mg alloys, tensile tests are conducted at both room temperature and 120 ℃. Subsequently, the resulting fractures are observed. The cross-sectional morphology of the fractures reveals that cracks in the Mg matrix primarily originate at incoherent phase boundaries, specifically the $Mg_{17}Al_{12}$ and $Al_8Mn_5$ phase boundaries. These cracks then propagate along the phase boundaries, leading to a transgranular cleavage fracture of the Mg matrix. The ultimate tensile strength (UTS) and elongation (ε) to failure of this alloy is found to be 170 MPa and 11.8%, respectively. The source of cracking is indicated by yellow arrows in Figure 14(c). The presence of typical cleavage planes and fracture steps in the fracture (Figure 14(a)) highly supports this deduction.

Interestingly, the cross-section of the fracture depicted in Figure 15(d) indicates that Mg-Y alloys exhibit similar cracking behavior at these incoherent phase boundaries. The EDS and BSE results in Figure 15(e, f) provide

additional evidence supporting the aforementioned conclusion, as $Mg_{17}Al_{12}$ and $Al_8Mn_5$ are observed on the fracture surface. Considering the weak bonding of incoherent phase boundaries and the sharp shapes of the $Al_8Mn_5$ and $Mg_{17}Al_{12}$ intermetallics, the preferential cracking at these boundaries is well interpreted. It is worth noting that this phenomenon persists even though the intermetallic compounds experience refinement upon the addition of Y; however, cracking is not observed at the $Al_8Mn_4Y$ phase boundaries. As a result, both the UTS and ε of the alloy comprise 0.4 wt.% Y increase, with elongation to failure (ε) reaching, 23.7% and UTS reaching 201 MPa. These findings indicate that the effects resulting from Y addition, such as morphological optimization of the IMCs, the formation of $Al_8Mn_4Y$ particles, and the resulting semi-coherent boundaries generated in the alloy, contribute to the enhancement of both strength and elongation.

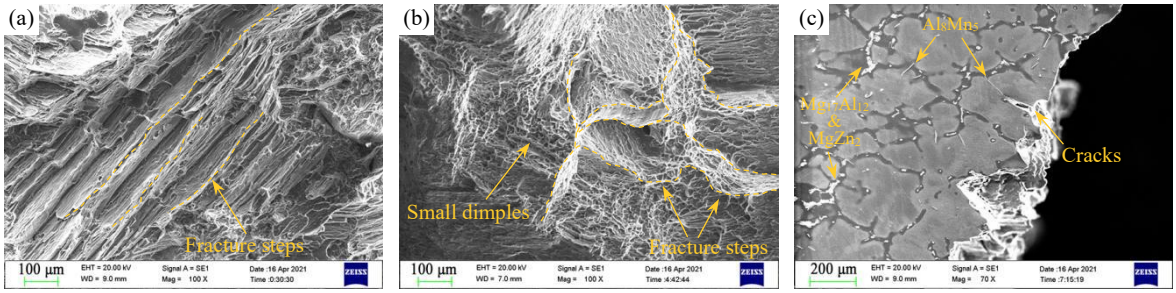


**Figure 14: Fracture of the Mg alloy matrix. (a, b) room- and elevated-temperature fractures, (c) cross-sectional morphology of the room-temperature fracture.**

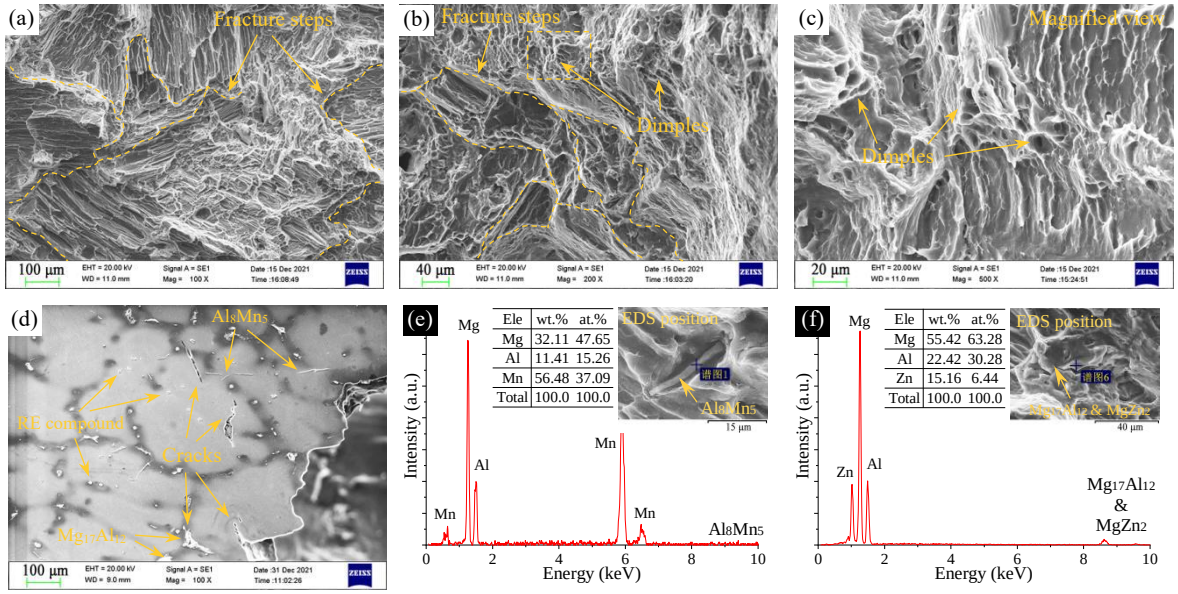


**Figure 15: Fracture of the sample containing 0.4 wt.% Y. (a, b) room- and elevated-temperature fractures, (c) magnified view of the dimples in the elevated-temperature fracture, (d) cross-section of the room-temperature fracture, (e, f) EDS results of $Mg_{17}Al_{12}$&$MgZn_2$ eutectic and $Al_8Mn_5$ on the fracture.**

The ductility of Mg alloys improves with increasing temperatures, due to the decreasing CRSS required for the slip initiation at elevated temperatures. Consequently, dimples can be observed in both Y-free and Y-containing samples that fracture at elevated temperatures. This observation indicates a quasi-cleavage fracture mode, as shown in Figure 14(b) and Figure 15(b, c). It is evident that the thermal softening diminishes the lattice resistance to dislocation motion within the Mg matrix and conventional IMCs (like $Mg_{17}Al_{12}$). As a result, the elongation to failure of the Mg matrix increases dramatically, reaching 40.8 %. Meanwhile, the UTS decreases to 118 MPa, demonstrating the typical thermal softening of the alloy. The stress-strain curves of the Mg alloy matrix are depicted in Figure 17(b).

It is noteworthy that RE intermetallics possess thermal stability. As a result, the elastic modulus difference between

RE intermetallics (such as $Al_8Mn_4Y$ and $Al_2Y$) and the Mg matrix increases with rising temperatures. At elevated temperatures, dislocations within the Mg matrix are pinned by the RE intermetallics, resulting in minimal fluctuation in the mechanical properties of the alloy. The UTS and ε are retained at 190 MPa and 27.1%, respectively.

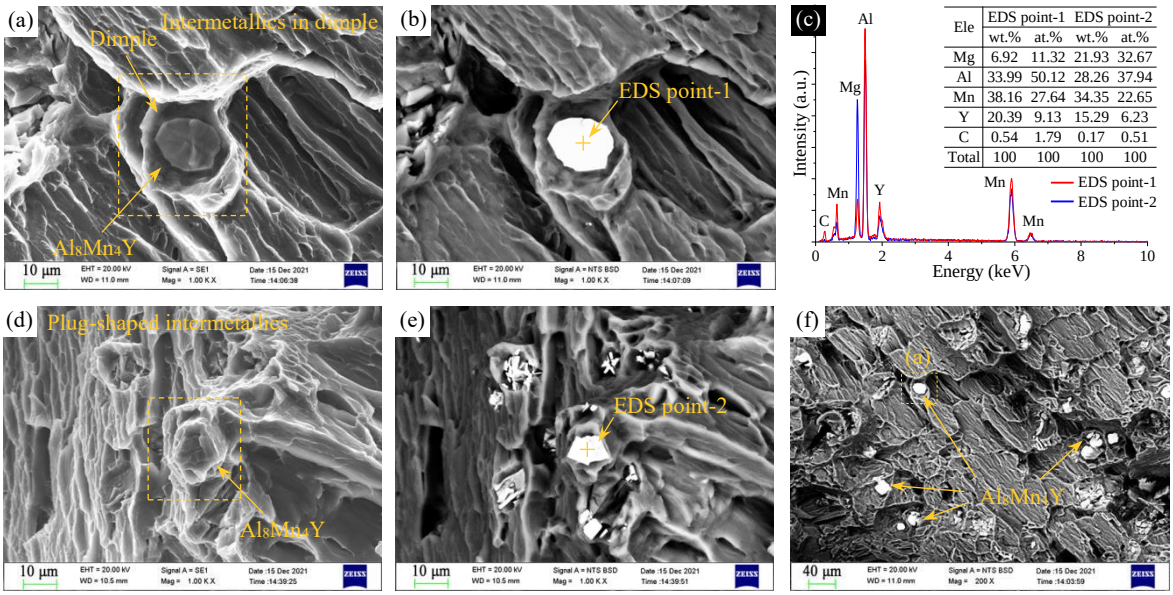


| Ele | EDS point-1 | | EDS point-2 | |
|---|---|---|---|---|
| | wt.% | at.% | wt.% | at.% |
| Mg | 6.92 | 11.32 | 21.93 | 32.67 |
| Al | 33.99 | 50.12 | 28.26 | 37.94 |
| Mn | 38.16 | 27.64 | 34.35 | 22.65 |
| Y | 20.39 | 9.13 | 15.29 | 6.23 |
| C | 0.54 | 1.79 | 0.17 | 0.51 |
| Total | 100 | 100 | 100 | 100 |

**Figure 16: Elevated temperature fracture of the sample comprising 0.4 wt.% Y. (a, b) SEM and BSE images of the plug-shaped intermetallics in the fracture, (c) EDS results of the bright contrast intermetallics on the surface of fracture, (d) SEM image of intermetallics in the dimple, (e) BSE image of the dimple, (f) distribution of $Al_8Mn_4Y$ in the fracture.**

Notably, stress concentrations at $Al_8Mn_4Y$ intensify during the deformation of the alloy. Consequently, fractures occur within the $Al_8Mn_4Y$ particles or at the relevant phase boundaries, forming dimples centered around $Al_8Mn_4Y$, as shown in Figure 16(a, d). This deduction finds robust support in the fracture observations and elemental analysis depicted in Figure 16, demonstrating that the lattice of the Mg matrix is pinned by the $Al_8Mn_4Y$ particles at both room and elevated temperatures. Therefore, to enhance the ductility and prevent cracking of Mg alloys at elevated temperatures, it is crucial to refine the large-sized IMCs originally present in the alloy, with a particular emphasis on generating IMCs that are coherent/semi-coherent with the Mg matrix. This approach serves to alleviate stress concentrations at phase boundaries and effectively immobilize dislocations during alloy deformation, both at room and elevated temperatures.

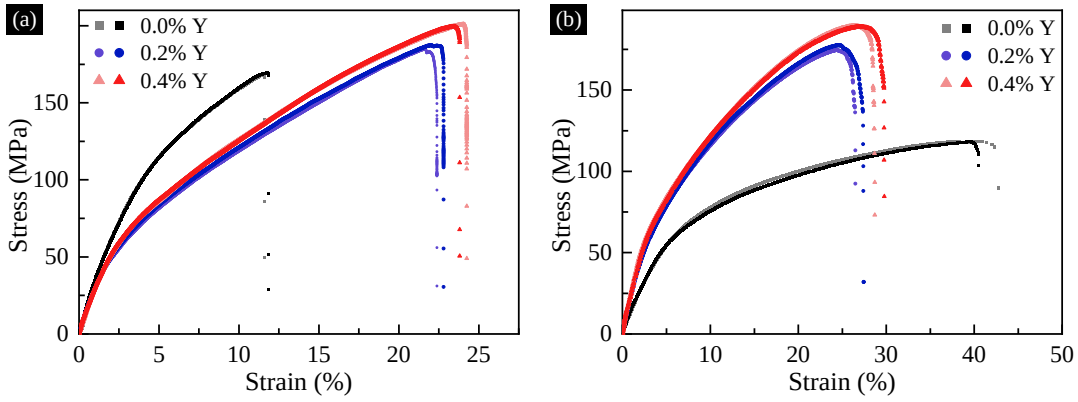


**Figure 17: Tensile curves of the matrix and samples containing Y. Results obtained at (a) room and (b) elevated temperatures.**

The aforementioned findings highlight the role of Y element in Mg alloys, particularly the effects originating from the $Al_8Mn_4Y$ intermetallic compound. These effects encompass an almost two-fold increase in the elongation of

the Mg alloy matrix following the addition of a moderate amount of Y. Furthermore, the reduction in elongation at elevated temperatures for Y-containing samples is minor. The tensile test results presented in Figure 17 and Table 3 strongly support the discussion regarding the role of the Y element in Mg alloys.

**Table 3: UTS and ε values of the samples with and without Y**

| **Sample** | | **Room temperature** | | | | | | **Elevated temperature (120 ℃)** | | | | | |
|---|---|---|---|---|---|---|---|---|---|---|---|---|---|
| | | **UTS (MPa)** | | | **ε (%)** | | | **UTS (MPa)** | | | **ε (%)** | | |
| | | Values | Avg. | SD | Values | Avg. | SD | Values | Avg. | SD | Values | Avg. | SD |
| **Mg alloy matrix (Y-free sample)** | No. 1 | 170.21 | 169.64 | 0.81 | 11.83 | 11.75 | 0.11 | 117.88 | 118.43 | 0.77 | 39.87 | 40.76 | 1.25 |
| | No. 2 | 169.06 | | | 11.67 | | | 118.97 | | | 41.64 | | |
| **Sample containing 0.2 wt.% Y** | No. 1 | 185.29 | 186.34 | 1.48 | 21.73 | 22.17 | 0.62 | 178.25 | 176.83 | 2.02 | 24.86 | 24.66 | 0.28 |
| | No. 2 | 187.38 | | | 22.61 | | | 175.40 | | | 24.46 | | |
| **Sample containing 0.4 wt.% Y** | No. 1 | 202.12 | 201.34 | 1.11 | 24.05 | 23.76 | 0.42 | 189.23 | 189.84 | 0.86 | 27.51 | 27.08 | 0.61 |
| | No. 2 | 200.55 | | | 23.46 | | | 190.45 | | | 26.65 | | |

## 3.5 Mechanical properties of $Al_8Mn_4Y$ intermetallic compound

Nanoindentation is employed to assess the mechanical properties of $Al_8Mn_4Y$, with a specific focus on hardness and elastic modulus. This approach facilitated a comparative analysis of the contributions of $Al_8Mn_4Y$ and $Mg_{17}Al_{12}$ to the mechanical properties of Mg alloys. The indentation sites and their corresponding hardness values are depicted in Figure 18. The outcomes reveal that the average hardness of $Al_8Mn_4Y$ is 4.647 GPa, significantly higher than that of $Mg_{17}Al_{12}$ (3.163 GPa) and approximately seven times that of the Mg matrix (0.645 GPa). Notably, the hardness values obtained for $Mg_{17}Al_{12}$ and the Mg matrix in this study closely align with those reported in the existing literature [44, 45], thus highlighting the reliability of nanoindentation as a technique for quantifying the mechanical properties of $Al_8Mn_4Y$.

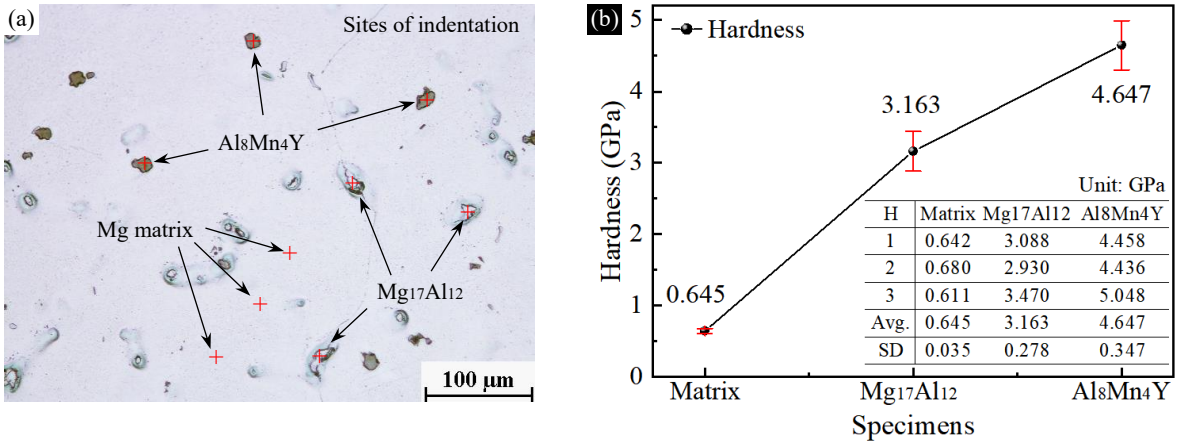

| H | Matrix | Mg17Al12 | Al8Mn4Y |
|---|---|---|---|
| 1 | 0.642 | 3.088 | 4.458 |
| 2 | 0.680 | 2.930 | 4.436 |
| 3 | 0.611 | 3.470 | 5.048 |
| Avg. | 0.645 | 3.163 | 4.647 |
| SD | 0.035 | 0.278 | 0.347 |

**Figure 18: Hardness of intermetallic compounds within the alloy. (a) indentation sites, (b) hardness values.**

The load-depth curves are illustrated in Figure 14(a). The elastic modulus was determined using the Oliver-Pharr method [46], as expressed in Equation 2, where $E_r$ represents the reduced elastic modulus, $E$ and v denote the elastic modulus and Poisson ratio of the sample, and $E_i$ and $v_i$ stand for the elastic modulus and Poisson ratio of the indenter.

$$\frac{1}{E_r}=\frac{1-v^2}{E}+\frac{1-v_i^2}{E_i} \cdots\cdots\cdots\cdots 2$$

According to studies [45, 47], the Poisson ratios of $Mg_{17}Al_{12}$ and α-Mg are reported as 0.24 [45] and 0.29 [47], respectively. Furthermore, the values for $v_i$ and $E_i$ of the Berkovich indenter are 0.07 and 1141 GPa [47], respectively. With the reduced modulus ($E_r$) of $Mg_{17}Al_{12}$ and the Mg matrix measuring 69.921 and 43.723 GPa in this work, the corresponding elastic modulus ($E$) is determined to be 70.178 and 41.634 GPa, respectively. These findings are in agreement with those reported by Wróbel et al. [48], Lu et al. [49], and Yang et al. [50].

It is important to note that the Poisson ratio of $Al_8Mn_4Y$ has not been previously reported. Therefore, material computation (CASTEP method) was employed to predict the Poisson ratio, yielding a value of 0.227 for $Al_8Mn_4Y$. This calculated result closely aligns with those obtained in other Al-X-Y (X = Cu, Zr) intermetallic compounds. For instance, the reported Poisson ratios for $Al_8Cu_4Y$ [50] and $Al_8Cr_4Y$ [50] are 0.243 [50] and 0.237 [50], respectively. Consequently, the *E* of $Al_8Mn_4Y$ is determined, with an average value of 124.421 GPa. Notably, this study makes the first experimental measurement of the hardness and elastic modulus of $Al_8Mn_4Y$ in Mg alloys.

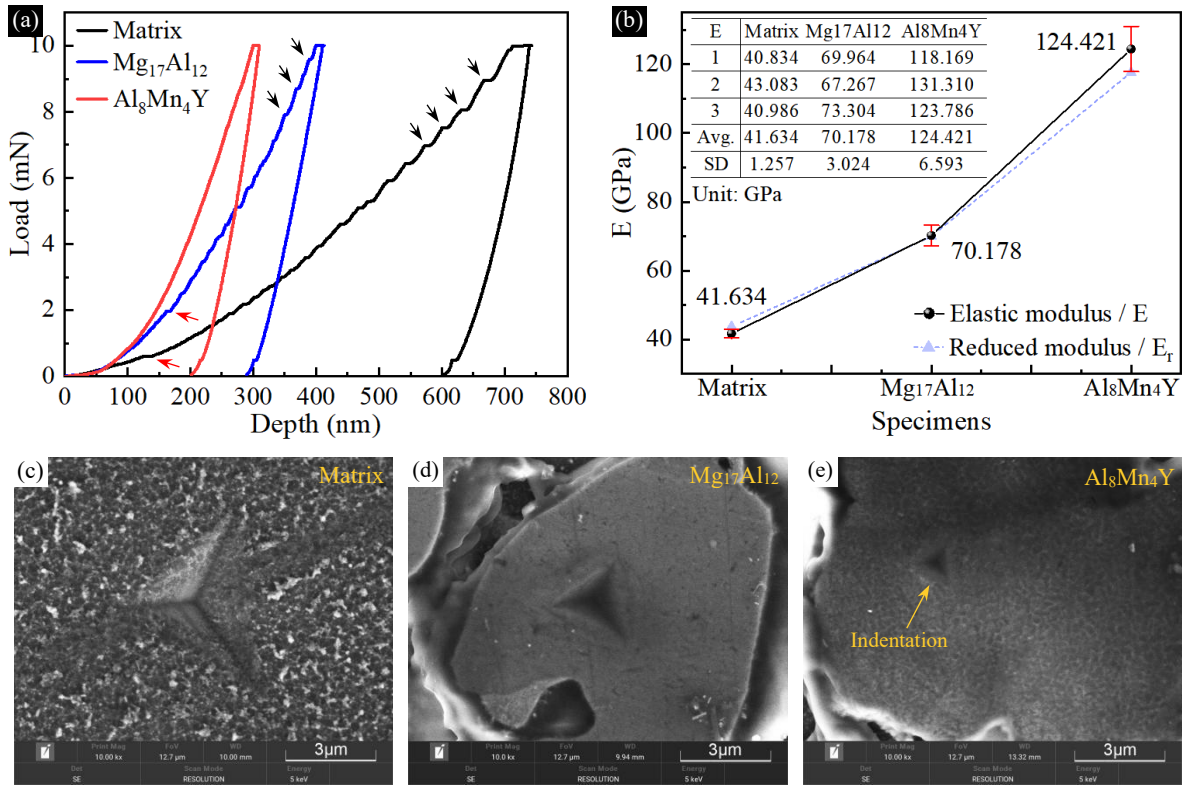


| E | Matrix | $Mg_{17}Al_{12}$ | $Al_8Mn_4Y$ |
|---|---|---|---|
| 1 | 40.834 | 69.964 | 118.169 |
| 2 | 43.083 | 67.267 | 131.310 |
| 3 | 40.986 | 73.304 | 123.786 |
| Avg. | 41.634 | 70.178 | 124.421 |
| SD | 1.257 | 3.024 | 6.593 |

Unit: GPa

**Figure 19: Load-depth curves and indentations. (a) load-depth curves, (b) elastic moduli, (c, d, e) indentations of the Mg matrix, $Mg_{17}Al_{12}$, and $Al_8Mn_4Y$.**

It is widely acknowledged that load-depth curves provide valuable insights into lattice responses during deformation [51]. Upon comparing the load-depth curves in Figure 19(a), it becomes evident that both $Mg_{17}Al_{12}$ and Mg matrix lattices readily initiate slip, as evidenced by the presence of typical serrations (i.e., pop-in events) at the initial section of the loading segment. The first serration emerges in the Mg matrix curve at a load of 0.6 mN, while for $Mg_{17}Al_{12}$, it appears at approximately 2 mN. Notably, the displacement of these serrations increases with the rising load, as indicated by the arrows in Figure 19(a). In contrast, the curve for $Al_8Mn_4Y$ appears smoother, devoid of serrations within the loading segment.

Mathur et al. [45] analyzed pop-in events in their indention studies of $Mg_{17}Al_{12}$ and attributed them to lattice slip, indicating that these pop-in events mark the transition from elastic to plastic deformation. Similarly, Bradby et al. [52] concluded that the pop-in event signifies the sudden yielding of the alloy. Therefore, it can be inferred that $Mg_{17}Al_{12}$ helps alleviate stress concentration at phase boundaries during alloy deformation through its own slip mechanism. This effect is particularly pronounced at elevated temperatures, as $Mg_{17}Al_{12}$ softens at temperatures above 120 ℃. This finding is supported by the tensile tests conducted at 120 ℃ and the corresponding fracture analysis, suggesting a limited pinning effect of $Mg_{17}Al_{12}$, particularly at elevated temperatures. In contrast, the slip behavior of the $Al_8Mn_4Y$ lattice remains linear and well-coordinated, even under higher loads (Figure 14(a)). Consequently, dislocations in $Al_8Mn_4Y$ nucleate uniformly within the high-stress field of the lattice. These characteristics enable $Al_8Mn_4Y$ intermetallics, which form strong bonds with the Mg matrix through their semi-

coherent boundaries, to serve as effective barriers against the slip of the Mg matrix.

## 3.6 Effect of Y on elastic and plastic deformation of the alloy

### *3.6.1 At room temperature*

The impact of Y on the yield strength ($\sigma_y$) of Mg alloys can be quantified using four individual contributions [53]: intrinsic lattice frictional stress ($\sigma_0$), grain boundary ($\Delta\sigma_{GB}$), dislocation ($\Delta\sigma_\rho$), and precipitation ($\Delta\sigma_{PS}$), as demonstrated in Equation 3.

It is important to emphasize that the combination of $\sigma_0$ and $\Delta\sigma_{GB}$ corresponds to the classical Hall-Petch relation [54]: $\sigma_y = \sigma_0 + k_y/(d)^{-1/2}$

Accordingly, the increase in $\sigma_y$ due to grain boundary strengthening is characterized by $\Delta\sigma_{GB} = k_y/(d)^{-1/2}$, where $k_y$ represents the influence coefficient of the grain boundary on $\sigma_y$ (a weakly temperature-dependent constant), and $d$ is the average grain size [55].

$$\begin{cases} \sigma_y = \sigma_0 + \Delta\sigma_{GB} + \Delta\sigma_\rho + \Delta\sigma_P \\ \Delta\sigma_{GB} = k_y / \sqrt{d} \\ \Delta\sigma_\rho = MaGb\sqrt{\rho} \\ \Delta\sigma_{Orowan} = M \dfrac{0.4Gb}{\pi\sqrt{1-\nu}} \dfrac{\ln(2\bar{r}/b)}{\lambda} \end{cases} \quad \cdots\cdots\cdots\cdots\cdots\cdots\cdots\cdots\cdots\cdots \quad 3$$

Microstructural observations in Section 3.1 reveal that grains in samples containing 0.2~0.4 wt.% Y are refined, compared to those in Y-free samples. However, the $\sigma_y$ values of samples containing Y are slightly lower than that of the Mg matrix at room temperature. The aforementioned findings contradict the Hall-Petch relation, indicating that $\Delta\sigma_\rho$ and $\Delta\sigma_{PS}$ play dominant roles in determining the yield strength in this case.

$\Delta\sigma_\rho$ can be quantified using the well-known Taylor equation: $\Delta\sigma_\rho = MaGb(\rho)^{1/2}$ [56]. Here, $M$ represents the Taylor factor (a constant), $a$ is a constant for HCP alloys, $G$ is the shear modulus, $b$ is the Burgers vector, and $\rho$ is the dislocation density. It is evident that $\Delta\sigma_\rho$ depends strongly on $\rho$. However, at the macroscopic scale, the number of IMCs in the alloy decreases after the addition of Y, as shown in Figure 1. Notably, semi-coherent boundaries are formed between $Al_8Mn_4Y$ intermetallics and the Mg matrix. As a result, the original dislocation density ($\rho_{original}$) present in the as-cast alloy decreases, while dynamic dislocations ($\rho_{dynamic}$) have not yet formed during the elastic deformation of the alloy. This implies that less energy is required for the elastic deformation of the alloy following the addition of Y. Consequently, the contribution of dislocation strengthening to the $\sigma_y$ of the alloy decreases.

It is a challenge for dislocations to penetrate or shear large-sized intermetallic compounds. Consequently, dislocation motion halts at phase boundaries [57], leading to the pile-up of dislocations around the IMCs and their eventual by-passing. This phenomenon is known as the Orowan by-passing mechanism [58, 59], which elucidates the mechanisms behind pinning. Therefore, the value of $\Delta\sigma_{PS}$ is quantified using the Orowan-Ashby equation [60]: $\Delta\sigma_{Orowan} = 0.4MGb\cdot ln(2\bar{r}/b)\cdot(\pi\lambda(1-\nu)^{1/2})^{-1}$ (shown in Equation 3). Here, $\nu$ represents the Poisson ratio of the matrix, $\bar{r}$ is the average equivalent radius of the IMCs, and $\lambda$ is the average spacing between IMCs. It is now evident that $\Delta\sigma_{PS}$ is determined by the distribution of IMCs within the grains, since $M$, $G$, and $\nu$ are material-related constants. Considering that the total number of IMCs within the alloy decreases after the addition of Y (which means a decreasing distributional density) the contribution of $\Delta\sigma_{PS}$ is correspondingly diminished.

$$\begin{cases} \Delta\sigma_{PS} = K^{-1}\Delta\sigma_{PS-Spherical} \\ K = h^{\frac{1}{6}}\left(\dfrac{2+h^2}{3}\right)^{-\frac{1}{4}} \\ h = c/a \end{cases} \quad \cdots\cdots\cdots\cdots\cdots\cdots\cdots\cdots\cdots\cdots \quad 4$$

Notably, the Orowan-Ashby equation assumes that all intermetallics possess ideal spherical morphologies.

Therefore, a correction factor ($K$) is introduced to adapt the approach for rod- or island-shaped intermetallics. This adaptation is formalized in Equation 4 [61]. Here, $K$ is the correction factor, $h$ represents the aspect ratio of the intermetallics, $a$ and $c$ respectively denote the diameter and height of the rod-like intermetallics. For non-spherical intermetallics, $h = c/a > 1$. Accordingly, the functional analysis of $K = h^{1/6}((2 + h^2) / 3)^{-1/4}$ reveals that $K \leq 1$ and $K^{-1} \geq 1$, as depicted in Fig. 20. Consequently, it is evident that spherical IMCs (i.e., particles) exert the weakest influence as barriers against the elastic deformation of the alloy.

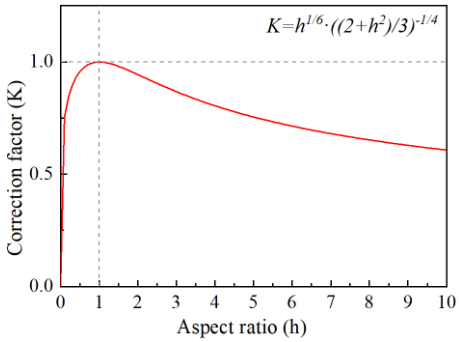

**Fig. 20 Functional relation between $K$ and $h$.**

Furthermore, the formation of $Al_8Mn_4Y$ particles and the refinement of initially large-sized intermetallics within the alloy further diminish the contribution of $\Delta\sigma_{PS}$, resulting in a slight decrease in $\sigma_y$ of the alloy. Notably, the presence of granular intermetallics reduces the deformation stress and minimizes cracking tendencies at phase boundaries, contributing to the enhancement of the strength and plasticity of the alloy.

### *3.6.2 At elevated temperatures*

Similarly, the impact of Y on the elastic deformation of the alloy at elevated temperatures is elucidated. Lattice frictional stress ($\sigma_0$) is actually the Peierls-Nabarro force, which exhibits a pronounced temperature dependency [62]. It is evident that $\sigma_0$ diminishes with rising temperatures [63]. Additionally, the $E$ values for both α-Mg and $Mg_{17}Al_{12}$ decrease at elevated temperatures, along with their corresponding shear modulus ($G$), because $G = E / 2(1 + v)$. Earlier investigations [64] have demonstrated that the $E$ of pure Mg at 100 °C is merely 70% of its room temperature value. A comparable trend is observed for $Mg_{17}Al_{12}$. Consequently, the contribution of dislocation strengthening ($\Delta\sigma_p$) and precipitation strengthening ($\Delta\sigma_{PS}$) to the $\sigma_y$ of the alloy decreases significantly at elevated temperatures. This decline is attributed to the linear dependence of $\Delta\sigma_p$ and $\Delta\sigma_{PS}$ on $G$, as highlighted by Equation 3.

$$\begin{cases} k_y = M^2 \tau_c r^{1/2} \\ \tau_c = Be^{-\beta T} \end{cases} \quad \cdots\cdots \quad 5$$

Notably, higher temperatures elevate atoms to a higher energy state, facilitating their departure from equilibrium positions. As a result, the impedance posed by grain boundaries diminishes. Yu et al. [65] and Ono et al. [63] quantified the Hall-Petch slope, $k_y$, using Equation 5, where $M$ represents the Taylor orientation factor, $\tau_c$ signifies the CRSS of a specific deformation mode, $r$ indicates the distance from the dislocation pile-up to the nearest dislocation source in the adjacent grain, $B$ and $\beta$ are constants at a fixed strain rate, and $T$ denotes absolute temperature. $B$ decreases with increasing strain rate, whereas $M$ and $r$ remain material-specific constants [65]. As a result, $k_y$ is primarily dictated by $\tau_c$. Moreover, higher temperatures correspond to lower $\tau_c$ and $k_y$ values. This approach unveils the substantial attenuation of grain boundary strengthening ($\Delta\sigma_{GB}$) at elevated temperatures, since $\Delta\sigma_{GB}$ is determined using $\Delta\sigma_{GB} = k_y / (d)^{-1/2}$. Therefore, $\sigma_y$ of the Y-free sample decreases sharply at elevated temperatures is supported by the tensile test results.

It is important to note that the above approach only considers the contribution of grain boundaries themselves, disregarding the pinning effect originating from IMCs within the grain boundaries. In fact, $Mg_{17}Al_{12}$ within grain boundaries softens at elevated temperatures, leading to a weakening of its hindrance to lattice deformation. In contrast, semi-coherent boundaries possess lower interfacial energy, and $Al_8Mn_4Y$ itself exhibits thermal stability. The hindrance imposed by Y-containing intermetallics on the alloy lattice remains high even at elevated temperatures. These discussions further elucidate the strengthening effects of semi-coherent boundaries and the $Al_8Mn_4Y$ intermetallics on Mg alloys. It should also be noted that the refined conventional intermetallics and the newly generated Y-containing particles are dispersed throughout the grain boundaries and grains, resulting in multiple reinforcement mechanisms. As a result, the reduction in the yield strength of the Y-containing sample at elevated temperatures is minimal.

### *3.6.3 Plastic deformation*

The thermal softening of conventional intermetallics at elevated temperatures, coupled with their refinement following the addition of Y, helps alleviate stress concentration at both phase and grain boundaries during the elastic/plastic deformation. As a result, the cracking potential of the Y-containing sample is reduced under both room and elevated temperatures. Notably, nanoindentation studies have revealed that both $Mg_{17}Al_{12}$ and α-Mg lattices are susceptible to slipping. This characteristic enables $Mg_{17}Al_{12}$ to coordinate the deformation of the Mg matrix through its own slip, particularly at elevated temperatures. Consequently, the corresponding dynamic dislocation density ($\rho_{dynamic}$) nucleated within the alloy during the plastic deformation is reduced. These two mechanisms contribute to an enhancement in the elongation of the alloy [66].

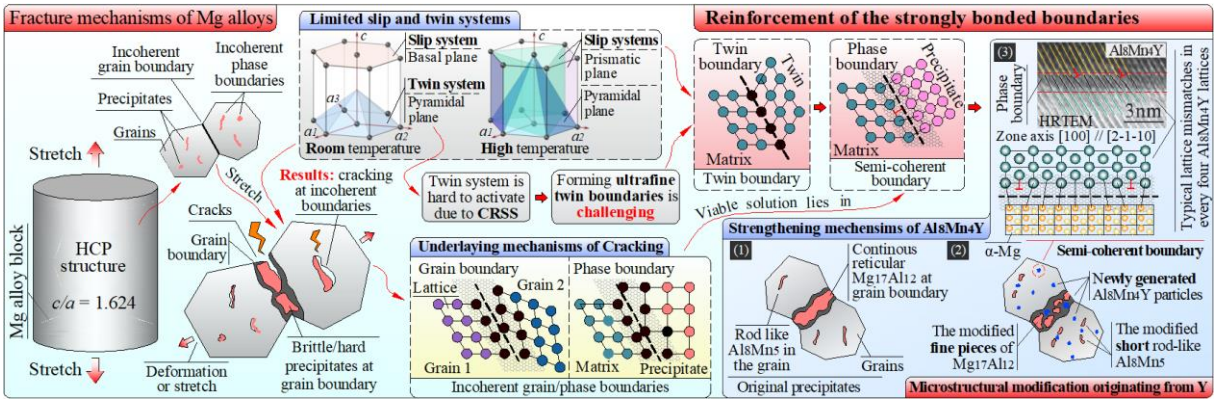


**Figure 21: Schematic diagram of the strengthening mechanisms of simi-coherent boundaries.**

It is worth noting that both $Al_8Mn_4Y$ and $Al_2Y$ exhibit thermal stability. Furthermore, $Al_8Mn_4Y$ intermetallics form strong bonds with the Mg matrix through their semi-coherent boundaries. These characteristics suggest a reduced stress concentration at phase boundaries upon the formation of $Al_8Mn_4Y$. Additionally, during the plastic deformation of the alloy, the motion of dislocations is impeded by IMCs (including the newly generated Y-containing particles and the refined conventional intermetallics) within the alloy. This leads to an increased number of dislocations nucleating from the pinning sites, driven by the intense deformation of the Mg matrix. As a result, the alloy experiences further hardening. The mechanisms behind the lattice slip of the Mg matrix and the strengthening arising from semi-coherent boundaries are illustrated in Figure 21. By considering the experimental findings of this study, it becomes evident that the enhancement of both grain boundaries and the Mg matrix plays a pivotal role in concurrently improving the strength and plasticity of the alloy.

## 5 Conclusion

In this work, we have presented a novel method to enhance the bonding between intermetallics and the matrix by forming semi-coherent boundaries. By employing different materials characterization techniques, a previously unexplored intermetallic compound (IMC), $Al_8Mn_4Y$, has been identified and systematically investigated. Main

outcomes of this investigation are summarized below.

- The microstructural and compositional analysis reveals that the addition of an appropriate quantity of Y not only refines originally inherited intermetallic compounds within the alloy but also generates Y-containing particles. The primary intermetallic compounds in the novel Mg-Al-Zn-Mn-Y system include $Al_8Mn_4Y$, $Al_8Mn_5$, $Mg_{17}Al_{12}$, $MgZn_2$, and $Al_2Y$.
- $Al_8Mn_4Y$ is observed using HRTEM and SAED, which revealed lattice parameters of $a = b = 8.929$ Å and $c = 5.095$ Å. To the best of authors knowledge, this marks the first accurate calibration of $Al_8Mn_4Y$ using experimental methods.
- HRTEM observations revealed that $Al_8Mn_4Y$ exhibits semi-coherence with the Mg matrix at their phase boundaries. Typical lattice mismatches are observable for every four $Al_8Mn_4Y$ lattices along the $<010>_{Al8Mn4Y}$ direction. Theoretical lattice mismatch calculations validate the experimental results, identifying at least four sets of plane pairs with mismatches lower than 6%. These findings establish $Al_8Mn_4Y$ as the first reported intermetallic compound in Mg alloys that demonstrates semi-coherence with the α-Mg at room temperature.
- Nanoindentation test results reveal that the hardness and $E$ of $Al_8Mn_4Y$ are significantly higher than those of $Mg_{17}Al_{12}$, measuring 4.647 GPa and 124.421 GPa, respectively. The load-depth curves suggest that α-Mg and $Mg_{17}Al_{12}$ lattices are susceptible to slipping, while the slip behavior of the $Al_8Mn_4Y$ lattice remains linear and well-coordinated even under higher load. These characteristics enable $Al_8Mn_4Y$ to effectively anchor both the lattices of the Mg matrix and the grain boundaries, thereby enhancing the strength of the alloy.
- Tensile test and fracture analysis demonstrate that cracking at incoherent phase boundaries is the dominant failure mode of Mg alloys. The refinement of conventional intermetallics and the introduction of semi-coherent boundaries resulting from the formation of $Al_8Mn_4Y$ help alleviate stress concentration at both phase and grain boundaries, contributing to the ductility improvement of the alloy.
- The effects of Y on the elastic and plastic deformation of Mg alloys were quantified using four individual contributions: intrinsic lattice frictional stress ($\sigma_0$), grain boundary ($\Delta\sigma_{GB}$), dislocation ($\Delta\sigma_\rho$), and precipitation ($\Delta\sigma_{PS}$). Accordingly, the underlying mechanisms behind the simultaneous enhancement of strength and ductility in Mg alloys are elucidated, offering valuable insights into the design strategies for future Mg alloys.

## Declaration of Competing Interest

The authors declare that they have no known competing financial interests or personal relationships that could have appeared to influence the work reported in this paper.

## Acknowledgment

This work was supported by (1) Key Research and Development Program of Jiangxi Province (No.20203BBG73070); (2) Natural Science Foundation of Jiangxi Province-General Project (No.20202BABA204009); (3) National Natural Science Foundation of China (No.51861024)

## References

[1] Ogawa Y, Ando D, Sutou Y, et al. A lightweight shape-memory magnesium alloy[J]. Science, 2016,353(6297):368-370.

[2] Wu Z, Curtin W A. The origins of high hardening and low ductility in magnesium[J]. Nature, 2015,526(7571):62-67.

[3] Song J, She J, Chen D, et al. Latest research advances on magnesium and magnesium alloys worldwide[J]. Journal of Magnesium and Alloys, 2020,8(1):1-41.
[4] Wei K, Hu R, Yin D, et al. Grain size effect on tensile properties and slip systems of pure magnesium[J]. Acta Materialia, 2021,206:116604.
[5] Kumar N R, Blandin J J, Suery M, et al. Effect of alloying elements on the ignition resistance of magnesium alloys[J]. Scripta materialia, 2003,49(3):225-230.
[6] Lu N, Du K, Lu L, et al. Transition of dislocation nucleation induced by local stress concentration in nanotwinned copper[J]. Nature communications, 2015,6(1):7648.
[7] Tang S, Xin T, Xu W, et al. Precipitation strengthening in an ultralight magnesium alloy[J]. Nature communications, 2019,10(1):1003.
[8] Bayani H, Saebnoori E. Effect of rare earth elements addition on thermal fatigue behaviors of AZ91 magnesium alloy[J]. Journal of Rare Earths, 2009,27(2):255-258.
[9] Ragani J, Donnadieu P, Tassin C, et al. High-temperature deformation of the γ-Mg17Al12 complex metallic alloy[J]. Scripta Materialia, 2011,65(3):253-256.
[10] Srinivasan A, Ajithkumar K K, Swaminathan J, et al. Creep behavior of AZ91 magnesium alloy[J]. Procedia Engineering, 2013,55:109-113.
[11] Xu S W, Kamado S, Matsumoto N, et al. Recrystallization mechanism of as-cast AZ91 magnesium alloy during hot compressive deformation[J]. Materials Science and Engineering: A, 2009,527(1-2):52-60.
[12] Zúberová Z, Kunz L, Lamark T T, et al. Fatigue and tensile behavior of cast, hot-rolled, and severely plastically deformed AZ31 magnesium alloy[J]. Metallurgical and Materials Transactions A, 2007,38:1934-1940.
[13] Wang Y, Xia M, Fan Z, et al. The effect of Al8Mn5 intermetallic particles on grain size of as-cast Mg–Al–Zn AZ91D alloy[J]. Intermetallics, 2010,18(8):1683-1689.
[14] Pan F, Feng Z, Zhang X, et al. The types and distribution characterization of Al-Mn phases in the AZ61 magnesium alloy[J]. Procedia Engineering, 2012,27:833-839.
[15] Sarvesha R, Thirunavukkarasu G, Chiu Y L, et al. A study on the phase transformation of γ2-Al8Mn5 to LT-Al11Mn4 during solutionizing in AZ91 alloy[J]. Journal of Alloys and Compounds, 2021,873:159836.
[16] Zhang X, Zhang Q, Hu H. Tensile behaviour and microstructure of magnesium AM60-based hybrid composite containing Al2O3 fibres and particles[J]. Materials Science and Engineering: A, 2014,607:269-276.
[17] Srinivasan A, Swaminathan J, Gunjan M K, et al. Effect of intermetallic phases on the creep behavior of AZ91 magnesium alloy[J]. Materials Science and Engineering: A, 2010,527(6):1395-1403.
[18] Li Q, Wang Q, Wang Y, et al. Effect of Nd and Y addition on microstructure and mechanical properties of as-cast Mg–Zn–Zr alloy[J]. Journal of Alloys and Compounds, 2007,427(1-2):115-123.
[19] Mo N, Tan Q, Bermingham M, et al. Current development of creep-resistant magnesium cast alloys: A review[J]. Materials & Design, 2018,155:422-442.
[20] Zhou Y, Luo Q, Jiang B, et al. Strength-ductility synergy in Mg98. 3Y1. 3Ni0. 4 alloy processed by high temperature homogenization and rolling[J]. Scripta Materialia, 2022,208:114345.
[21] Xu W, Zhang B, Li X Y, et al. Suppressing atomic diffusion with the Schwarz crystal structure in supersaturated Al–Mg alloys[J]. Science, 2021,373(6555):683-687.
[22] Song G, Sun Z, Li L, et al. Ferritic alloys with extreme creep resistance via coherent hierarchical precipitates[J]. Scientific reports, 2015,5(1):16327.
[23] Jiang S, Wang H, Wu Y, et al. Ultrastrong steel via minimal lattice misfit and high-density nanoprecipitation[J]. Nature, 2017,544(7651):460-464.
[24] Karnesky R A, Meng L, Dunand D C. Strengthening mechanisms in aluminum containing coherent Al3Sc precipitates and incoherent Al2O3 dispersoids[J]. Acta Materialia, 2007,55(4):1299-1308.

[25] Ming K, Bi X, Wang J. Realizing strength-ductility combination of coarse-grained Al0. 2Co1. 5CrFeNi1. 5Ti0. 3 alloy via nano-sized, coherent precipitates[J]. International Journal of Plasticity, 2018,100:177-191.
[26] Wen H, Zhao B, Dong X, et al. Preferential growth of coherent precipitates at grain boundary[J]. Materials Letters, 2020,261:126984.
[27] Lu K, Lu L, Suresh S. Strengthening materials by engineering coherent internal boundaries at the nanoscale[J]. science, 2009,324(5925):349-352.
[28] Koike J, Kobayashi T, Mukai T, et al. The activity of non-basal slip systems and dynamic recovery at room temperature in fine-grained AZ31B magnesium alloys[J]. Acta materialia, 2003,51(7):2055-2065.
[29] Burssík J, Svoboda M. A HREM and analytical STEM study of precipitates in an AZ91 magnesium alloy[J]. Microchimica Acta, 2002,139:39-42.
[30] Zhou X, Yan H, Chen J, et al. Effects of the β1′ precipitates on mechanical and damping properties of ZK60 magnesium alloy[J]. Materials Science and Engineering: A, 2021,804:140730.
[31] Hänzi A C, Dalla Torre F H, Sologubenko A S, et al. Design strategy for microalloyed ultra-ductile magnesium alloys[J]. Philosophical Magazine Letters, 2009,89(6):377-390.
[32] Xiaofeng N, Zhiwei H, Han W, et al. Structure, Elastic Properties, Thermodynamic and Electronic Properties of Al-Y Alloy Under Pressure from First-principles Calculations[J]. Rare Metal Materials and Engineering, 2018,47(5):1325-1332.
[33] Chen Y, Zhu Z, Zhou J. Study on the strengthening mechanism of rare earth yttrium on magnesium alloys[J]. Materials Science and Engineering: A, 2022,850:143513.
[34] Chen Y, Zhu Z, Zhou J, et al. Identification of Intermetallics in the Laser-Welded Joint of Rare-Earth Magnesium Alloy and the Corresponding Strengthening Mechanisms[J]. Journal of Materials Research and Technology, 2023.
[35] Liu X J, Ohnuma I, Kainuma R, et al. Thermodynamic assessment of the Aluminum-Manganese (Al-Mn) binary phase diagram[J]. Journal of phase equilibria, 1999,20:45-56.
[36] Lu L, Chen X, Huang X, et al. Revealing the maximum strength in nanotwinned copper[J]. Science, 2009,323(5914):607-610.
[37] Du Y, Wang J, Zhao J, et al. Reassessment of the Al–Mn system and a thermodynamic description of the Al–Mg–Mn system[J]. International journal of materials research, 2007,98(9):855-871.
[38] Huang L, Liu S, Du Y, et al. Thermal conductivity of the Mg–Al–Zn alloys: Experimental measurement and CALPHAD modeling[J]. Calphad, 2018,62:99-108.
[39] Doi M. Elasticity effects on the microstructure of alloys containing coherent precipitates[J]. Progress in Materials Science, 1996,40(2):79-180.
[40] Gao X, He S M, Zeng X Q, et al. Microstructure evolution in a Mg–15Gd–0.5 Zr (wt.%) alloy during isothermal aging at 250 C[J]. Materials Science and Engineering: A, 2006,431(1-2):322-327.
[41] Nishijima M, Yubuta K, Hiraga K. Characterization of β′ precipitate phase in Mg-2 at% Y alloy aged to peak hardness condition by high-angle annular detector dark-field scanning transmission electron microscopy (HAADF-STEM)[J]. Materials transactions, 2007,48(1):84-87.
[42] Pineau A. Influence of uniaxial stress on the morphology of coherent precipitates during coarsening—elastic energy considerations[J]. Acta metallurgica, 1976,24(6):559-564.
[43] Wang N, Ji Y, Wang Y, et al. Two modes of grain boundary pinning by coherent precipitates[J]. Acta Materialia, 2017,135:226-232.
[44] Sarvesha R, Alam W, Gokhale A, et al. Quantitative assessment of second phase particles characteristics and its role on the deformation response of a Mg-8Al-0.5 Zn alloy[J]. Materials Science and Engineering: A, 2019,759:368-379.
[45] Mathur H N, Maier-Kiener V, Korte-Kerzel S. Deformation in the γ-Mg17Al12 phase at 25–278 C[J]. Acta materialia, 2016,113:221-229.

[46] Durst K, Backes B, Franke O, et al. Indentation size effect in metallic materials: Modeling strength from pop-in to macroscopic hardness using geometrically necessary dislocations[J]. Acta Materialia, 2006,54(9):2547-2555.
[47] Zhang M, Huang H, Spencer K, et al. Nanomechanics of Mg–Al intermetallic compounds[J]. Surface and Coatings Technology, 2010,204(14):2118-2122.
[48] Wróbel J, Hector Jr L G, Wolf W, et al. Thermodynamic and mechanical properties of lanthanum–magnesium phases from density functional theory[J]. Journal of alloys and compounds, 2012,512(1):296-310.
[49] Lu Y, Gharghouri M, Taheri F, et al. Numerical study of the casting features on the fracture and debonding of Mg17Al12 in AM60B Mg alloy under high cycle fatigue condition[J]. Materials & design, 2009,30(6):1994-2005.
[50] Yang W, Pang M, Tan Y, et al. A comparative first-principles study on electronic structures and mechanical properties of ternary intermetallic compounds Al8Cr4Y and Al8Cu4Y: Pressure and tension effects[J]. Journal of Physics and Chemistry of Solids, 2016,98:298-308.
[51] Somekawa H, Tsuru T, Singh A, et al. Effect of crystal orientation on incipient plasticity during nanoindentation of magnesium[J]. Acta Materialia, 2017,139:21-29.
[52] Bradby J E, Williams J S, Swain M V. Pop-in events induced by spherical indentation in compound semiconductors[J]. Journal of Materials research, 2004,19(1):380-386.
[53] Jang T J, Choi W S, Kim D W, et al. Shear band-driven precipitate dispersion for ultrastrong ductile medium-entropy alloys[J]. Nature communications, 2021,12(1):4703.
[54] Zhao M, Li J C, Jiang Q. Hall–Petch relationship in nanometer size range[J]. Journal of alloys and compounds, 2003,361(1-2):160-164.
[55] Cordero Z C, Knight B E, Schuh C A. Six decades of the Hall–Petch effect–a survey of grain-size strengthening studies on pure metals[J]. International Materials Reviews, 2016,61(8):495-512.
[56] Schouwenaars R. A statistical analysis of strain hardening: The percolation limit and the Taylor equation[J]. Acta materialia, 2012,60(18):6331-6340.
[57] Aragon N K, Gravell J D, Ryu I. Dislocation interactions at the grain boundary in FCC bicrystals: An atomistically-informed dislocation dynamics study[J]. Acta Materialia, 2022,223:117455.
[58] Liu L, Zhang Y, Han J, et al. Nanoprecipitate-strengthened high-entropy alloys[J]. Advanced Science, 2021,8(23):2100870.
[59] Nandy S, Ray K K, Das D. Process model to predict yield strength of AA6063 alloy[J]. Materials Science and Engineering: A, 2015,644:413-424.
[60] Correia J B, Davies H A, Sellars C M. Strengthening in rapidly solidified age hardened Cu□ Cr and Cu□ Cr□ Zr alloys[J]. Acta Materialia, 1997,45(1):177-190.
[61] Sonderegger B, Kozeschnik E. Particle strengthening in fcc crystals with prolate and oblate precipitates[J]. Scripta Materialia, 2012,66(1):52-55.
[62] Bata V, Pereloma E V. An alternative physical explanation of the Hall–Petch relation[J]. Acta materialia, 2004,52(3):657-665.
[63] Ono N, Nowak R, Miura S. Effect of deformation temperature on Hall–Petch relationship registered for polycrystalline magnesium[J]. Materials Letters, 2004,58(1-2):39-43.
[64] Garlea E, Radovic M, Liaw P K. High-temperature dependency of elastic mechanical behavior of two wrought magnesium alloys AZ31B and ZK60A studied by resonant ultrasound spectroscopy[J]. Materials Science and Engineering: A, 2019,758:86-95.
[65] Yu H, Xin Y, Wang M, et al. Hall-Petch relationship in Mg alloys: A review[J]. Journal of Materials Science & Technology, 2018,34(2):248-256.
[66] Li Q. Mechanical properties and microscopic deformation mechanism of polycrystalline magnesium under high-strain-rate compressive loadings[J]. Materials Science and Engineering: A, 2012,540:130-134.